Engineering Structures 342 (2025) 120962

Contents lists available at ScienceDirect

Engineering Structures

journal homepage: www.elsevier.com/locate/engstruct

Analysis and design of slender square concrete-filled double-skin stainless steel tubular columns

M.F. Hassanein [a,b], Amr E.K. Mohamed [a,c], K.A. Cashell [d], Marina Bock [e], Yilinke Tan [a,*], Mohamed M.A. Hussein [c], Yong-Bo Shao [a]

[a] School of Architecture and Civil Engineering, Xihua University, Chengdu, Sichuan 610039, China
[b] Department of Structural Engineering, Faculty of Engineering, Tanta University, Tanta, Egypt
[c] Department of Civil Engineering, Faculty of Engineering, Sohag University, Sohag, Egypt
[d] Department of Civil Environmental and Geomatic Engineering, UCL, London, UK
[e] College of Engineering and Physical Sciences, Department of Civil Engineering, Aston University, Birmingham, UK

ARTICLE INFO

Keywords:
Stainless steel
Square tubes
CFDST
Slender columns
Global buckling
Finite element analysis
Axial design strength
Strength-to-weight ratio

ABSTRACT

This study investigates the structural behaviour and ultimate strength of slender square concrete-filled double-skin tubular (CFDST) columns comprising stainless steel outer tubes and carbon steel inner tubes. A validated finite element model was used to conduct an extensive parametric study examining the influence of slenderness, material properties, hollow ratio, and interfacial contact behaviour. The results highlight slenderness as the dominant factor affecting buckling resistance, with two slenderness thresholds proposed to delineate short, intermediate-length, and long columns. The slenderness ratio of the outer tube showed negligible effect on normalised strength and lateral deflection behaviour, confirming slenderness as the principal parameter controlling failure. Concrete strength notably influenced the post-peak response of intermediate-length columns but had minimal effect on long columns. The hollow ratio had a limited impact on axial strength but significantly improved the strength-to-weight ratio due to reduced column weight. Contact pressure analyses revealed maximum values at the section corners, decreasing with increased slenderness and reducing to zero at the mid-span of the sides. Among existing design provisions, AISC 360–16 demonstrated the greatest accuracy, with predictions typically within ±10 % of the finite element results. Existing design methods were evaluated, and two new design models are proposed, validated, and shown to provide improved accuracy and practical applicability for slender square CFDST columns. The proposed design models are presented in a simplified and practical format to facilitate ease of application in engineering practice, while providing a robust and reliable framework for structural design.

1. Introduction

Columns are essential members in many structural applications as they transfer vertical loads to the foundations and provide overall stability and strength by resisting both compression and bending forces. A particular type of column that has gained attention in recent years is the concrete-filled double-skin tubular (CFDST) column, which comprises two concentric steel tubes with concrete infill in the region between the two sections [1]. These columns have seen growing application in high-rise buildings and other structures subjected to heavy compressive loads [2]. Such applications are regularly found in marine, off-shore and industrial settings where durability and thermal resistance are other significant challenges, as well as the heavy loads. In response, researchers have studied the use of stainless steel for the outer steel section [3–10]. However, the behaviour of slender CFDST columns with a stainless steel outer section is much less studied. Researchers have investigated slender members but with a carbon steel outer sections, including under fire conditions [11–19].

* Corresponding author.
E-mail addresses: mostafa.fahmi@f-eng.tanta.edu.eg (M.F. Hassanein), amr.el_sayed@eng.sohag.edu.eg (A.E.K. Mohamed), k.cashell@ucl.uk (K.A. Cashell), m.bock@aston.ac.uk (M. Bock), tanyilinke@xhu.edu.cn (Y. Tan), mohamed.mahmoud2@eng.sohag.edu.eg (M.M.A. Hussein), shaoyb@mail.xhu.edu.cn (Y.-B. Shao).

https://doi.org/10.1016/j.engstruct.2025.120962
Received 22 May 2025; Received in revised form 20 June 2025; Accepted 12 July 2025
Available online 16 July 2025

Stainless steel has excellent structural properties, including outstanding load-bearing capacity, ductility [20] and exceptional durability [21] as well as fire resistance [19,22–24] and corrosion resistance [25,26]. As a result, many CFDST configurations have adopted a stainless steel outer tube and an inner carbon steel tube [4,5,7,8], making them particularly suitable for aggressive or marine environments. Recent studies have focused on the axial behaviour of square CFDST short columns with stainless steel outer tubes [4,5,7,10,27,28], due to their ease of integration with beams in building frames. However, while these short columns offer practical advantages, they are limited in their application. In real-world design scenarios [29,30], slender CFDST columns are more prevalent (as shown in Fig. 1). Unlike short columns, which typically fail due to local buckling of the steel tubes and crushing of the concrete core, slender columns tend to fail by overall (global) buckling. Accordingly, several recent studies have investigated the buckling performance of square composite slender columns with carbon steel tubes [31–36], with results evaluated against major design codes such as AISC 360–10 [37], AISC 360–16 [38], Eurocode 4 (EC4) [39], and AS/NZS 2327 [40]. While some of these studies have included advanced cross-sections (see Fig. 2), slender square CFDST columns with stainless steel outer tubes and carbon steel inner tubes remain unexamined.

It is important to note the different design approaches adopted by major codes. Only AISC [37] differentiates between elastic overall buckling (long columns) and inelastic buckling (intermediate-length columns), using separate hyperbolic and parabolic design curves with a non-dimensional slenderness limit of 1.5. In contrast, EC4 [39] and AS/NZS 2327 [40] apply a single design expression across the full slenderness range. EC4 is based on the Ayrton-Perry approach, incorporating equivalent imperfections and a plateau for non-dimensional slenderness values below 0.2 (for carbon steel) or 0.4 (for stainless steel) [41,42]. All three of these standards derive the design strength of slender composite columns from the plastic compressive resistance of the cross-section — a value recently calibrated for short square CFDST columns with stainless steel outer tubes [5]. However, the different approaches between the design codes warrant further investigation, particularly for slender composite members.

As stated before, the global buckling behaviour and design of slender square CFDST columns with stainless steel outer tubes and carbon steel inner tubes have not yet been studied. As such, to address this knowledge gap, the current paper proceeds with a description of a finite element model which was developed to investigate the axial compressive behaviour of such members (see Fig. 3). Following validation, the model was used to perform a parametric study, examining the influence of key parameters on the axial capacity of slender square CFDST columns. The ultimate strengths predicted by the FE simulations are compared with design strengths obtained using existing code provisions [38–40], and new design approaches are proposed in order to overcome deficiencies in the existing methods.

2. Finite element model

2.1. General

To investigate the axial compressive behaviour of slender square CFDST columns, a finite element (FE) model was developed using ABAQUS [43] to facilitate an extensive parametric study. A review of the literature reveals that experimental investigations specifically targeting this type of column are extremely limited. However, a number of relevant experimental studies on slender double-skin composite columns were identified and are used herein to validate the developed FE model. These include square concrete-filled dual tube steel tubular (CFDT) columns tested under axial compression [44], circular CFDT columns [36], square CFDST columns [45], and square concrete-filled stainless steel tubular (CFSST) columns [46]. Validation was carried out by comparing the predicted load–displacement behaviour and ultimate capacities obtained from the FE model with the corresponding experimental results.

2.2. Material modelling

The stress (σ_s)–strain (ε_s) behaviour of carbon steel was modelled using the five-stage constitutive model proposed by Han et al. [47,48], as shown in Fig. 4(a). This model has been widely adopted in previous studies [36,48] and was shown to accurately capture the mechanical response of carbon steel under compression. The stress–strain relationship is defined by the following equation:

$$\sigma_s = \begin{cases} E_s\varepsilon_s & \varepsilon_s \le \varepsilon_e \\ -A\varepsilon_s^2 + B\varepsilon_s + C & \varepsilon_e < \varepsilon_s \le \varepsilon_{e1} \\ f_y & \varepsilon_{e1} < \varepsilon_s \le \varepsilon_{e2} \\ f_y + \left(f_u - f_y\right)\dfrac{(\varepsilon_s - \varepsilon_{e2})}{(\varepsilon_{e3} - \varepsilon_{e2})} & \varepsilon_{e2} < \varepsilon_s \le \varepsilon_{e3} \\ f_u & \varepsilon_s > \varepsilon_{e3} \end{cases} \quad (1)$$

In this expression, E_s, f_y, and f_u are the elastic modulus, yield stress, and ultimate stress of steel, respectively, and with reference to Fig. 4(a), $\varepsilon_e = f_p/E_s$, $f_p = 0.8f_y$, $\varepsilon_{e1} = 1.5\varepsilon_e$, $\varepsilon_{e2} = 10\varepsilon_{e1}$, $\varepsilon_{e3} = 100\varepsilon_{e1}$, and the constants A, B and C are determined from: $A = 0.2f_y/(\varepsilon_{e1}-\varepsilon_e)^2$, $B = 2A\varepsilon_{e1}$, $C = 0.8f_y + A\varepsilon_e^2 - B\varepsilon_e$. The elastic modulus and Poisson's ratio of the carbon steel were taken as 210 GPa and 0.3, respectively.

For stainless steel, the two-stage Ramberg-Osgood (R-O) material model was adopted which is characterised by a gradual transition from elastic to plastic response [49–51]. This model effectively captures the rounded nature of the stress–strain curve, as illustrated in Fig. 4(b). The two-stage R–O model is defined using three fundamental parameters: the Young's modulus E_s, the yield strength f_y, and the strain-hardening exponent n. The stress–strain relationship for the R–O model is given

Fig. 1. Real-world applications of CFST and CFDST columns: (a) CFDST electricity pole [29], (b) CFST columns of Beijing Fortune Plaza [30] and (c) CFST columns of the terminal of Tianfu International Airport [30].

(a) Hassanein et al. [31] (b) Zhang et al. [32] (c) Hassanein et al. [33] (d) Chen et al. [34], Ahmed et al. [35] and Wang et al. [36]

Fig. 2. Square cross-sections considered in recent investigations on slender CFDST columns.

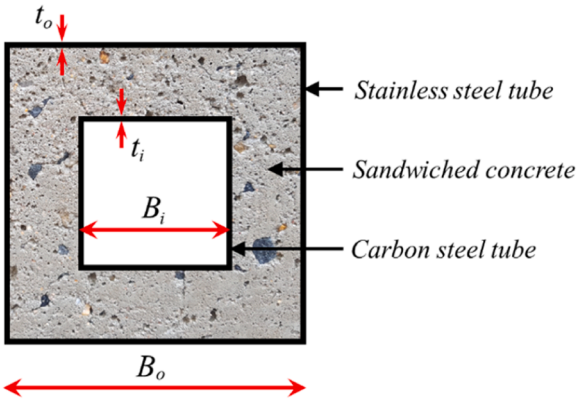

Fig. 3. Cross-section of Square-square CFDST column.

by Eq. (2):

$$\varepsilon_s = \begin{cases} \frac{f_s}{E_s} + 0.002\left(\frac{f_s}{f_y}\right)^n & \text{for } f_s \le f_y \\ \frac{f_s - f_y}{E_{0.2}} + \left(\varepsilon_u - \varepsilon_{0.2} - \frac{f_u - f_y}{E_{0.2}}\right)\left(\frac{f_s - f_u}{f_u - f_y}\right)^m & \text{for } f_y < f_s \le f_u \end{cases} \quad (2)$$

where f_u is the ultimate stress, ε_u is the ultimate strain (strain at f_u), f_y is the yield stress determined as the 0.2 % proof stress, $\varepsilon_{0.2}$ is the corresponding strain, $E_{0.2}$ is the tangent modulus of the stress-strain curve at the yield stress and n and m are the first and second strain hardening exponents, respectively, defined as given in Eq. (3) and Eq. (4) [50]:

$$n = \frac{\ln(20)}{\ln(f_y / f_{0.01})} \quad (3)$$

where $f_{0.01}$ is the 0.01 % proof stress

$$m = 1 + 2.8\frac{f_y}{f_u} \quad (4)$$

$E_{0.2}$, ε_u and f_u are determined as:

$$E_{0.2} = \frac{E_s}{1 + 0.002\, n \frac{E_s}{f_y}} \quad (5)$$

The ultimate strain is calculated using Eq. (6) [18]:

$$\varepsilon_u = 0.6\left(1 - \frac{f_y}{f_u}\right) \quad (6)$$

$$f_u = f_y\left(1 + \left(\frac{130}{f_y}\right)^{1.4}\right) \quad (7)$$

It is noteworthy that ABAQUS [43] requires the engineering stress σ_{eng} *versus* engineering strain ε_{eng} to be converted into true stress σ_{true} *versus* true plastic strain ε^{pl}_{true}, in accordance with the following expressions:

$$\sigma_{true} = \sigma_{eng.}(1 + \varepsilon_{eng.}) \quad (8)$$

$$\varepsilon^{pl}{}_{true} = \ln(1 + \varepsilon_{eng.}) - \frac{\sigma_{true}}{E_s} \quad (9)$$

The infill concrete was modelled using the concrete damaged plasticity (CDP) model available in ABAQUS. The CDP model is a widely used constitutive model for simulating the nonlinear behaviour of concrete under various loading conditions. It captures both tensile cracking and compressive crushing through separate damage mechanisms, allowing for a realistic representation of concrete's inelastic response. Tensile damage is characterised by the initiation and propagation of cracks, which reduce the material stiffness and lead to progressive degradation under increasing tensile strains. Compressive damage, on the other hand, reflects the material softening associated with crushing

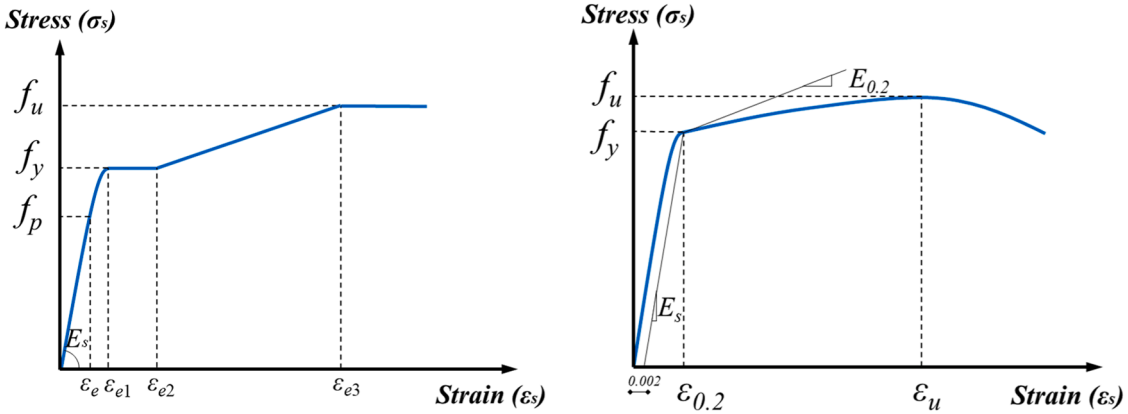

(a) Carbon steel (b) Stainless steel

Fig. 4. Stress-strain curve of steel material.

and localised failure under high compressive stress. The model incorporates lateral dilation, representing the volumetric expansion that occurs as concrete yields, particularly under confined or triaxial stress states. This dilation effect is governed by a non-associated flow rule, which helps simulate the pressure-dependent nature of concrete plasticity. Its ability to represent stiffness degradation and confinement effects makes it a powerful tool for capturing the complex failure mechanisms of concrete in both structural and material-level simulations. Herein, the uniaxial stress-strain relationship proposed by Han et al. [52] was adopted to represent the compressive behaviour of concrete, as illustrated in Fig. 5. This figure illustrates the evolution of the concrete stress-strain response during incremental loading. Initially, the response is linear elastic, followed by the onset of plastic deformation beyond strain ε_o, as predicted by the CDP model. As loading progresses, damage accumulates, and stiffness degradation becomes evident, leading to softening behaviour near peak stress. The elastic modulus of concrete was calculated using the ACI 318 [53] formula given as $E_c = 4700\sqrt{f_c'}$, where f_c' is the cylindrical compressive strength of concrete in MPa. The Poisson's ratio was taken as 0.2.

The CDP model requires the definition of five plasticity parameters, taken as follows: the dilation angle was taken as 40° for square sections, the flow potential eccentricity was 0.1, the biaxial-to-uniaxial compressive strength ratio was 1.16, the viscosity parameter was 1×10^{-5} and the stress invariant ratio (f_{bo}/f_{co}) was 0.667.

The compressive stress–strain behaviour of concrete was defined as:

$$\sigma_c = \begin{cases} \left[2\left(\frac{\varepsilon_c}{\varepsilon_o}\right) - \left(\frac{\varepsilon_c}{\varepsilon_o}\right)^2\right] f_c' & \varepsilon \le \varepsilon_o \\ \left[\frac{\varepsilon/\varepsilon_o}{\beta_o(\varepsilon/\varepsilon_o - 1)^{\eta} + \varepsilon/\varepsilon_o}\right] f_c' & \varepsilon > \varepsilon_o \end{cases} \quad (10)$$

where $\varepsilon_o = \varepsilon_c + 800\zeta^{0.2} \times 10^{-6}$ and $\varepsilon_c = (1300 + 12.5 f_c') \times 10^{-6}$. ζ is the confinement factor and was calculated as $\zeta = \frac{A_{so} f_{yo}}{A_c f_{ck}}$, A_{so} and A_c are the cross-sectional areas of the outer steel tube and concrete, respectively, f_{yo} is the yield stress of the outer stainless steel tube and f_{ck} is the characteristic strength of the concrete, corresponding to $0.67 f_{cu}$ for normal strength concrete, where f_{cu} is the cubic compressive strength of the concrete. The parameters η and β_o are defined as follows:

$$\eta = \begin{cases} 2 & \text{for circular sections} \\ 1.6 + \frac{1.5\varepsilon_o}{\varepsilon} & \text{for square sections} \end{cases} \quad (11)$$

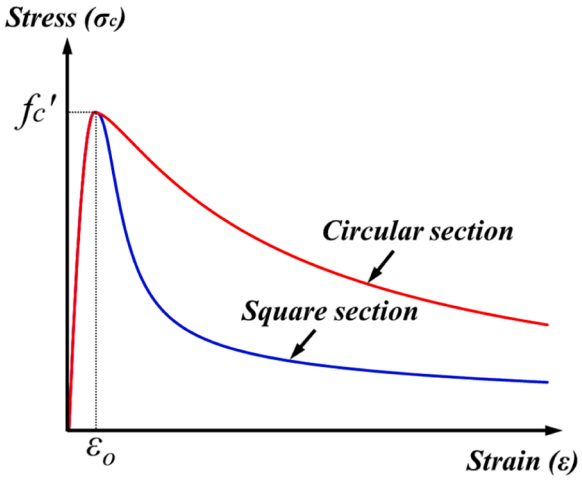

Fig. 5. Stress-strain curve of confined concrete material.

$$\beta_o = \begin{cases} 0.5\left(2.36 \times 10^{-5}\right)^{\left[0.25+(\zeta-0.5)^7\right]} (f_c')^{0.5} \ge 0.12 & \text{for circular sections} \\ \frac{(f_c')^{0.1}}{1.2\sqrt{1+\zeta}} & \text{for square sections} \end{cases} \quad (12)$$

For the tensile behaviour, a linear elastic response was assumed up to the tensile strength, followed by a softening branch governed by the fracture energy G_F. The tensile strength of concrete was taken as $0.1 f_c'$, and the fracture energy was calculated using:

$$G_F = \left(0.0469 d_{max}^2 - 0.5 d_{max} + 26\right)\left(\frac{f_c'}{10}\right)^{0.7} \ \text{N/m} \quad (13)$$

where d_{max} is the maximum nominal aggregate size, taken as 20 mm.

2.3. Interaction, boundary, and loading conditions

The surface-to-surface interaction approach was adopted to model the contact behaviour between the concrete infill and the steel tubes, as recommended by previous studies [33]. For the normal contact behaviour, the *hard contact* formulation was used. For the tangential contact, a Coulomb friction model was employed. The coefficient of friction was set to 0.6 for concrete-to-carbon steel contact [28,54] and 0.25 for concrete-to-stainless steel contact [55]. To replicate the boundary conditions of the physical tests and simulate the effective buckling length (L_e) of the columns, steel end plates were modelled at the top and bottom of the column. These end plates represented the pinned (triangular hinge) supports used in the experimental setups. Two reference points, denoted as RP1 (bottom) and RP2 (top), were introduced at the centroids of the respective end plates. The "Tie" constraint was applied to ensure full composite action between the steel tubes and the end plates, as well as between the concrete core and the steel plates. On the other hand, the "Coupling" constraint was used to link the two end plates with the reference points RP1 and RP2. At the bottom reference point (RP1), all translational and rotational degrees of freedom were restrained, except rotation about the x-axis, in order to allow for global buckling, which is characteristic of slender columns. At the top reference point (RP2), the x- and z-translations were fixed, while rotation about the x-axis remained unrestrained, maintaining symmetry and allowing buckling deformation. The axial compressive load was applied at the top of the column (RP2) through displacement-control, by imposing a vertical displacement of –15 mm in the direction of the column axis (U_2 direction). This approach allowed for the capture of post-peak behaviour. The overall boundary and loading conditions are illustrated in Fig. 6(a), which shows the configuration applied to the slender columns.

2.4. Mesh and solution procedure

The three-dimensional eight-noded linear brick element (C3D8R) was employed to simulate the steel tubes, infill concrete, and end plates. A mesh sensitivity study was conducted to achieve a balance between computational efficiency and result accuracy. Three mesh sizes — B_o/10, B_o/6, and B_o/5 — were evaluated in the analysis. Fig. 7 shows a comparison of the FE results obtained using these mesh sizes using specimen S1–3b [46]. The discrepancies between the FE and experimental ultimate loads for the B_o/10, B_o/6, and B_o/5 mesh sizes were 2 %, 5 %, and 3 %, respectively. However, the B_o/10 and B_o/5 meshes resulted in overestimated column stiffness values compared to B_o/6, as illustrated on the right-hand side of Fig. 7. Based on this study, the mesh size in the cross-sectional direction was set as B_o (or D_o)/6, while the mesh size along the longitudinal direction of the column was defined as twice the cross-sectional size. B_o and D_o are the outer width, or diameter, of the CFDST. The resulting mesh is shown in Fig. 6(b).

The analysis was performed in two main steps. First, a linear bucking

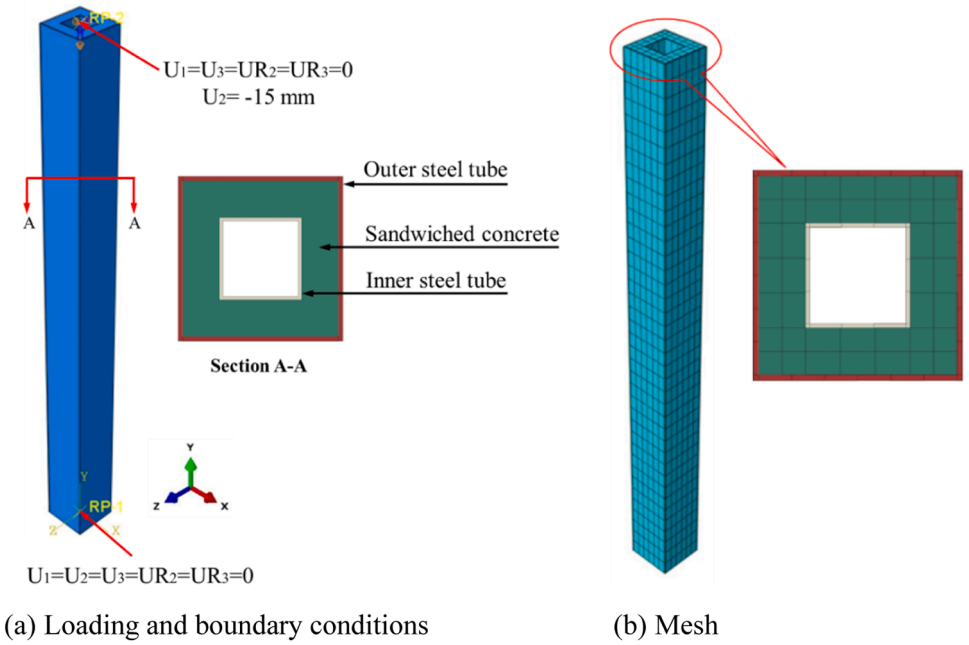

Fig. 6. Three-dimensional FE model of slender square–square CFDST columns.

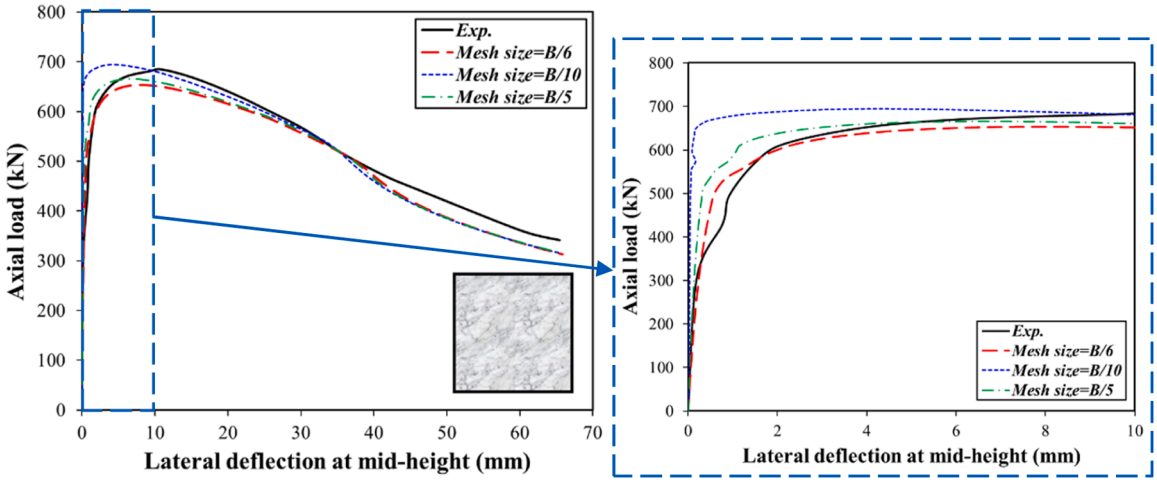

Fig. 7. Mesh sensitivity analysis for S1–3b [46].

analysis was conducted using the *"Buckle"* procedure in ABAQUS, which utilises an eigenvalue solver to determine the global buckling mode shapes. The first-mode shape from this step was subsequently used to define initial geometric imperfections in the second step, which was a nonlinear analysis. This involved a geometrically and materially nonlinear analysis using the *"Static, General"* procedure. To simulate global buckling failure, which is typical in slender columns, initial geometric imperfections were introduced into the model using the *"IMPERFECTION"* keyword. These imperfections were based on the buckling mode obtained in the first step and scaled appropriately.

For carbon steel columns, a global imperfection amplitude of L/1000 was adopted, following previous studies [32,36]. In contrast, for stainless steel columns, no universally accepted imperfection value exists. Hence, a parametric sensitivity study was carried out to determine the most appropriate imperfection amplitude. Four values were examined: $L/1000$, $L/5000$, $L/8000$, and $L/10000$. Fig. 8 presents a comparison between the FE predictions and experimental results for a square stainless steel CFST column using these values. The best agreement was found for $L/5000$, which was subsequently adopted in the model. This value is also supported by the findings of Hassanein and Kharoob [55] and An et al. [56]. To capture large deformation effects, the **nonlinear geometry option (NLGEOM)* was activated. The displacement increment settings were defined as 0.001 (initial), $1 \times 10^{-1\,5}$ (minimum), and 0.01 (maximum), and the total analysis time for the nonlinear step was set to 1.0.

2.5. Validation

The accuracy of the FE model was verified by comparing the numerical results against available experimental data. The validation focused on comparisons of axial load *versus* mid-height lateral deflection curves, ultimate axial load capacity, and the failure modes observed in both simulations and tests. Table 1 provides the geometric and material properties of the tested specimens, including the thicknesses of the outer and inner steel tubes, t_o and t_i, respectively, the widths (or diameters) of the outer and inner tubes, B_o (or D_o) and B_i (or D_i), respectively, the yield strengths of the outer and inner steel tubes, f_{yo} and f_{yi}, respectively, and the concrete compressive strengths f_c'. In the case where there is core

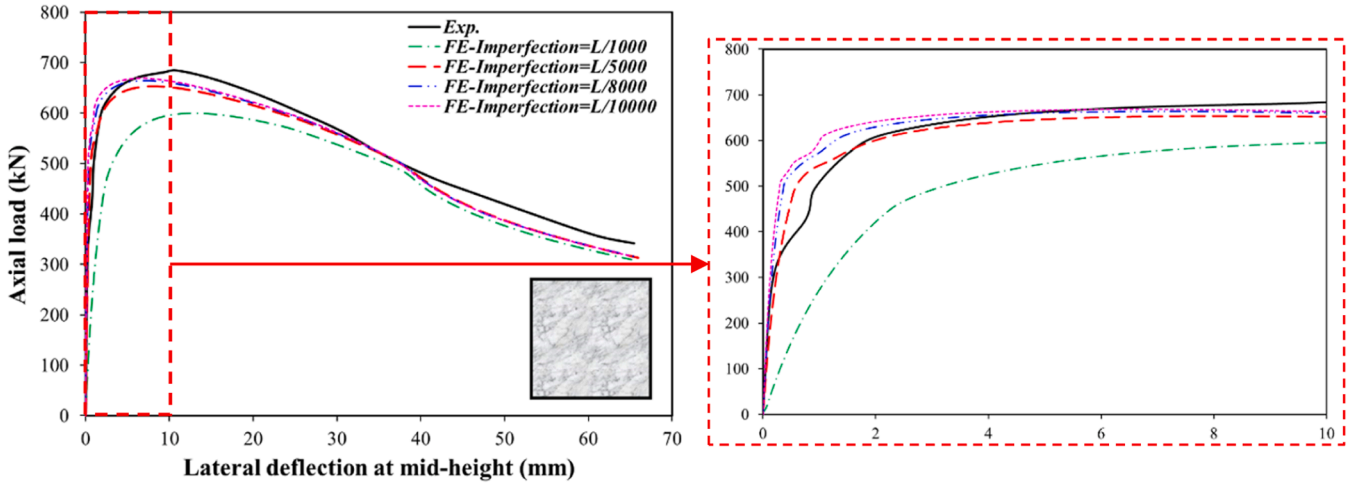

Fig. 8. Global imperfection sensitivity analysis of slender stainless steel columns.

Table 1
Dimensions and material properties of the slender columns.

Ref.	Specimen	D_o (B_o) (mm)	t_o (mm)	D_i (B_i) (mm)	t_i (mm)	L (mm)	λ	f_{yo} (MPa)	f_{yi} (MPa)	f_c' (f_{ci}') (MPa)
Carbon steel outer tube										
Zhu et al. [44]	L1200-C50-t4.4–6	200.0	4.40	120	4.35	1200	20.8	337.0	339.0	46.5 (34.9)
	L1600-C50-t4.4–8	200.0	4.40	120	4.35	1600	27.7	337.0	339.0	46.5 (34.9)
	L2000-C50-t4.4–10	200.0	4.40	120	4.35	2000	34.6	337.0	339.0	46.5 (34.9)
	L1600-C60-t4.4–8	200.0	4.40	120	4.35	1600	27.7	337.0	339.0	54.0 (34.9)
	L1600-C70-t4.4–8	200.0	4.40	120	4.35	1600	27.7	337.0	339.0	62.9 (34.9)
Wang et al. [36]	CCS1–1	127.0	3.00	48	1.90	1250	39.4	319.7	326.7	43.2
	CCS1–2	127.0	3.00	60	2.36	1250	39.4	319.7	336.2	43.2
	CCS1–3	127.0	3.00	48	1.90	1600	50.4	319.7	326.7	43.2
	CCS1–4	127.0	3.00	60	2.36	1600	50.4	319.7	336.2	43.2
	CCS2–1	140.0	3.00	48	1.90	1600	45.7	329.3	326.7	43.2
	CCS2–2	140.0	4.00	76	2.92	1600	45.7	309.5	311.9	43.2
	CCS2–3	140.0	4.00	76	3.75	1600	45.7	309.5	340.1	43.2
Han et al. [45]	scbc4–1	120.0	3.00	58	3.00	2136	58.0	275.9	374.5	39.1
	scbc4–2	120.0	3.00	58	3.00	2136	58.0	275.9	374.5	39.1
Stainless steel outer tube										
Uy et al. [46]	S1–1a	100.3	2.76	-	-	300	15.2	390.3	-	36.3
	S1–1b	100.3	2.76	-	-	300	15.2	390.3	-	75.4
	S1–2a	100.3	2.76	-	-	1200	46.3	390.3	-	36.3
	S1–2b	100.3	2.76	-	-	1200	46.3	390.3	-	75.4
	S1–3b	100.3	2.76	-	-	2400	87.7	390.3	-	75.4

concrete, the value of f_{ci}' is provided. Table 2 compares the ultimate axial loads obtained from the FE model ($N_{ult,FE}$) and the experimental tests ($N_{ult,Exp}$). The average $N_{ult,FE}/N_{ult,Exp}$ ratio for the slender composite columns was found to be 0.99, with a standard deviation of 0.051, indicating excellent agreement. Additionally, Fig. 9 illustrates the relationship between $N_{ult,FE}$ and $N_{ult,Exp}$, showing that all data points lie within a ± 10 % deviation band.

Further validation is presented in Fig. 10, where the numerical and experimental axial load–lateral deflection curves are compared. The numerical results closely match the experimental ones, particularly in terms of initial stiffness and overall structural response. This strong correlation confirms the model's ability to simulate the nonlinear behaviour of slender composite columns of different cross-section shapes under axial compression.

To validate the predicted failure modes, Fig. 11 and Fig. 12 compare the final deformed shapes of the outer and inner steel tubes and the concrete cores between the FE model and the test results of Wang et al. [36]. All circular specimens exhibited global buckling failure. Fig. 11(a) and Fig. 11(b) show the bending deformation of the outer and inner steel tubes, respectively, while Fig. 12 presents the deformation patterns and plastic strain distributions in the concrete cores. The FE model accurately captured the observed crushing and cracking zones in the concrete, demonstrating a high level of consistency with the experimental findings. Additional comparisons were made for square slender columns. Fig. 13 and Fig. 14 show the global buckling failure modes obtained from the FE model and experimental tests of Han et al. [45] and Uy et al. [46], respectively. The FE predictions successfully reproduced the global buckling shapes of square concrete-filled double-skin tubular (CFDST) specimens and square stainless steel tubular composite columns, further confirming the model's robustness.

To verify the material constitutive models used, an additional validation exercise was performed on short square CFDST columns with outer stainless steel tubes, using the experimental data from Wang et al. [4]. Table 3 summarises the properties of these specimens, while Table 4 compares the numerical and experimental ultimate loads. The average value of $N_{ult,FE}/N_{ult,Exp}$ was 1.01, with a standard deviation of 0.068, again showing strong agreement within a ± 10 % margin. The small discrepancies are attributed to the use of average concrete strengths from three test cylinders and other practical factors such as material variability. Also, comparisons between the FE and experimental axial load *versus* axial strain curves have been made to further ensure the accuracy of the FE model as shown in Fig. 15. A significant convergence between the curves was observed. However, the higher initial stiffness from FE simulations relative to the experimental curves arise from the

Table 2
Comparisons between FE and experimental load carrying capacities of slender CFDST columns.

Ref.	Specimen	$N_{ult,Exp.}$ (kN)	$N_{ult,FE.}$ (kN)	$N_{ult,FE}$ / $N_{ult,Exp.}$
Zhu et al. [44]	L1200-C50-t4.4–6	3267	3300	1.01
	L1600-C50-t4.4–8	3115	3245	1.04
	L2000-C50-t4.4–10	2913	3193	1.10
	L1600-C60-t4.4–8	3289	3409	1.04
	L1600-C70-t4.4–8	3515	3603	1.03
Wang et al. [36]	CCS1–1	840	849	1.01
	CCS1–2	956	892	0.93
	CCS1–3	760	797	1.05
	CCS1–4	820	839	1.02
	CCS2–1	1042	952	0.91
	CCS2–2	1120	1122	1.00
	CCS2–3	1160	1177	1.01
Han et al. [45]	scbc4–1	920	842	0.92
	scbc4–2	868	842	0.97
Uy et al. [46]	S1–1a	768	717	0.93
	S1–1b	1091	1063	0.97
	S1–2a	697	666	0.96
	S1–2b	1023	978	0.96
	S1–3b	684	653	0.95
Avg.				**0.99**
SD.				**0.051**

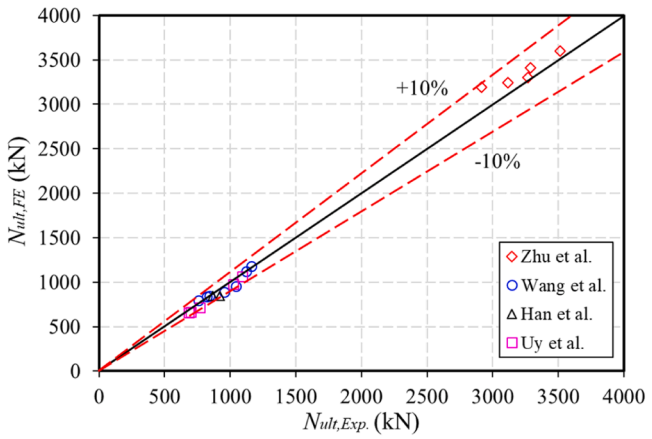

Fig. 9. Comparisons between $N_{ult,FE}$ and $N_{ult,Exp}$.

assumption of a uniform concrete compressive strength along the member's length and across its cross-section. Additionally, variations between the numerical and experimental results can be attributed to human errors during testing, slippage at the supports and loading points, as well as electrical interference affecting the strain gauge measurements. The experimental and FE failure modes of specimen LS100 × 3-NS40 × 1.5-C40 [4] are presented and compared in Fig. 16, together with the deformation and stress distribution in the concrete. Generally, the outward local buckling of the outer tube was accurately captured, demonstrating good agreement with the experimental test results. Moreover, concrete crushing was observed in the local buckling zones and near the corner regions of the square CFDST column specimen, as illustrated in Fig. 16(c).

3. Parametric study

The behaviour of different configurations of slender square CFDST columns with outer stainless steel tubes and inner carbon steel tubes were examined in a total of 90 FE simulations. The key parameters examined included the member slenderness (λ), width-to-thickness ratio of the outer steel tube (B_o/t_o), concrete cylindrical compressive strength (f_c') and section hollow ratio ($\overline{\chi}$). The materials used for the outer steel tubes were grades EN 1.4301 and EN 1.4318 austenitic stainless steels with 0.2 % proof strengths of 230 MPa and 350 MPa, respectively, and grade EN 1.4162 lean duplex stainless steel with a 0.2 % proof strength of 530 MPa [42]. For the inner steel tubes, S235 carbon steel was adopted, which had a yield and ultimate strengths of 235 MPa and 360 MPa, respectively [41]. The initial Young's modulus (E_o) was taken as 200 GPa for stainless steel and 210 GPa for carbon steel. A Poisson's ratio of 0.3 was used for all steel materials. Two grades of concrete were considered: 40 MPa normal strength concrete (NSC) and 80 MPa high strength concrete (HSC).

Three groups of columns (G1, G2, and G3), all using NSC, were created by varying the column length (L) and B_o/t_o. These variations provided a wide range of non-dimensional slenderness values ($\overline{\lambda}$), from 0.30 to 2.25, allowing for the determination of a slenderness limit (λ_r) that distinguishes between intermediate and long columns, and enabling evaluation of the effects of λ and B_o/t_o. The slenderness (λ) was determined as:

$$\lambda = \frac{Le}{\sqrt{I_{DS}/A_{DS}}} \tag{14}$$

where L_e is the effective buckling length, which was taken equal to the physical length (L) in the current study since all columns were modelled as pinned–pinned members. I_{DS} and A_{DS} denote the second moment of area and cross-sectional area of the entire composite column, respectively. The non-dimensional slenderness ($\overline{\lambda}$) was calculated in accordance with EC4 [39], as:

$$\overline{\lambda} = \sqrt{\frac{N_{pl,Rd}}{N_{cr}}} \tag{15}$$

Here, $N_{pl,Rd}$ is the plastic resistance of the CFDST column under axial compression, calculated following EC4 [39] and AS/NZS 2327 [40] as:

$$N_{pl,Rd} = A_{so,eff} f_{yo} + A_{sc} f_c' + A_{si} f_{yi} \tag{16}$$

In this expression, $A_{so,eff}$ is the effective area of the outer steel tube as defined in EC3 Part 1–5 [57], A_{sc} is the area of the sandwiched concrete and A_{si} is the area of the inner steel tube. The elastic critical load N_{cr} is determined using the effective flexural stiffness $(EI)_{eff}$ of the composite column, as given in EC4 [39]:

$$N_{cr} = \frac{\pi^2 (EI)_{eff}}{{L_e}^2} \tag{17}$$

$$(EI)_{eff} = E_{so} I_{so} + E_{si} I_{si} + 0.6 E_{sc} I_{sc} \tag{18}$$

where E_{so}, E_{si}, and E_{sc} are the moduli of elasticity of the outer stainless steel section, inner steel section, and sandwiched concrete, respectively. I_{so}, I_{si}, and I_{sc} are the second moments of area of the outer steel section, inner steel section, un-cracked sandwiched concrete section, respectively. The modulus for concrete E_{sc} is estimated using the empirical expression of EC2 [58]:

$$E_{sc} = 22000[(f_c'+8)/10]^{0.3} \text{ in MPa} \tag{19}$$

In addition to the initial three groups, six further groups (G4–G9) comprising intermediate-length and long CFDST columns were simulated. These groups include both compact and slender outer steel tubes and were developed to investigate the influence of concrete compressive strength (f_c'), yield strength of the outer tube (f_{yo}), and the section hollow ratio ($\overline{\chi}$). The ranges of studied parameters and the geometric and material properties of the FE models are summarised in Table 5 and Table A (in Appendix A), respectively. $\overline{\chi}$ as presented in Table 5 is calculated as $\overline{\chi} = \frac{B_i}{B_o - 2t_o}$.

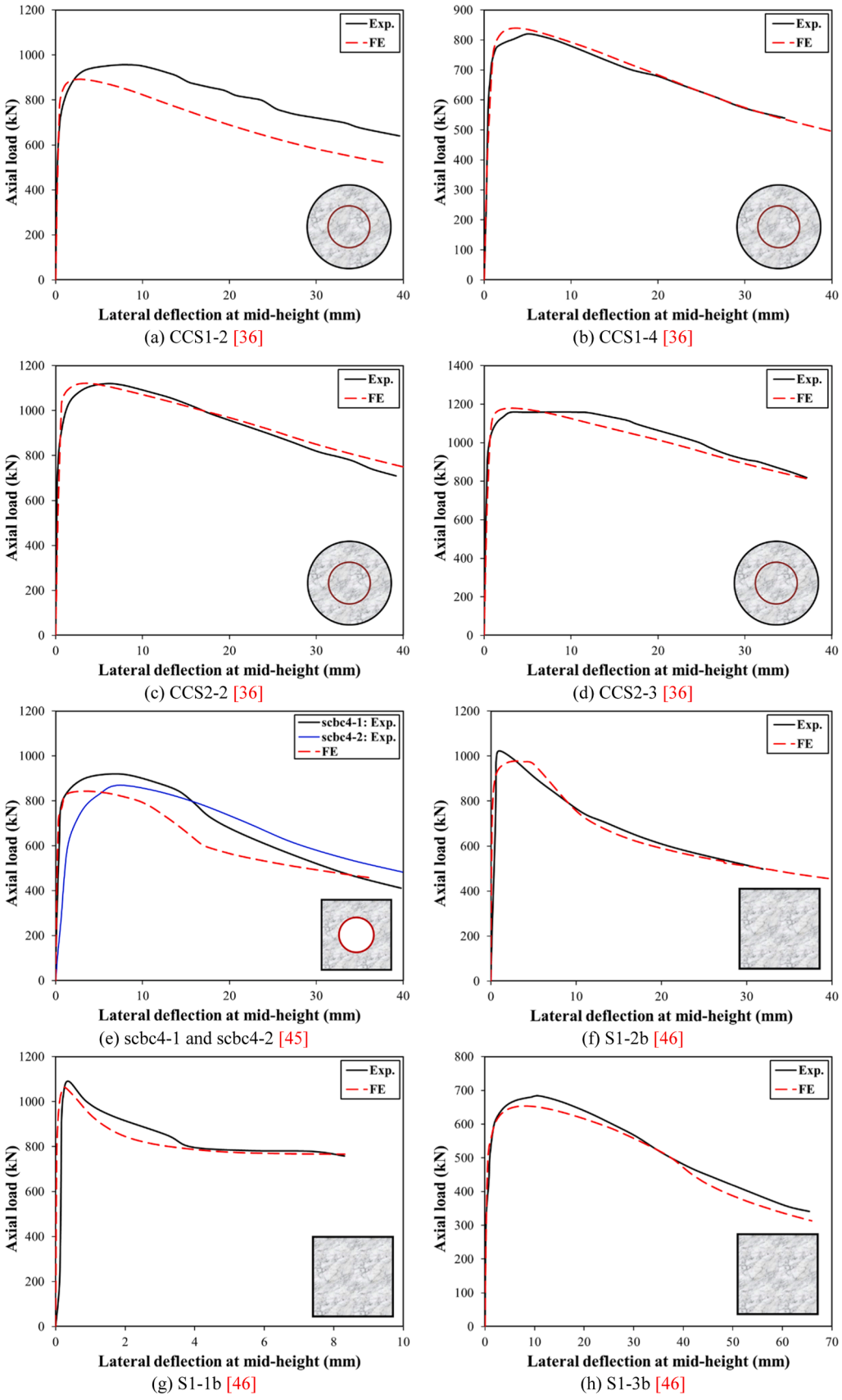

Fig. 10. Axial load ($N_{ult.}$) *versus* mid-height lateral deflection (u_m) of slender specimens.

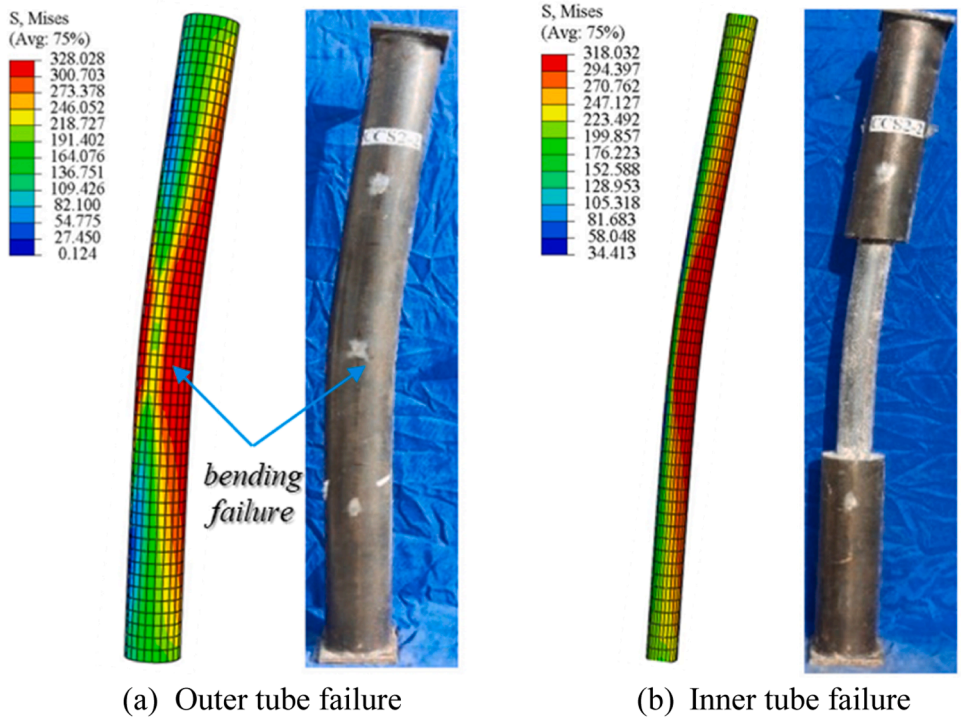

Fig. 11. Comparisons of the failure modes between the FE model and experimental tests [36].

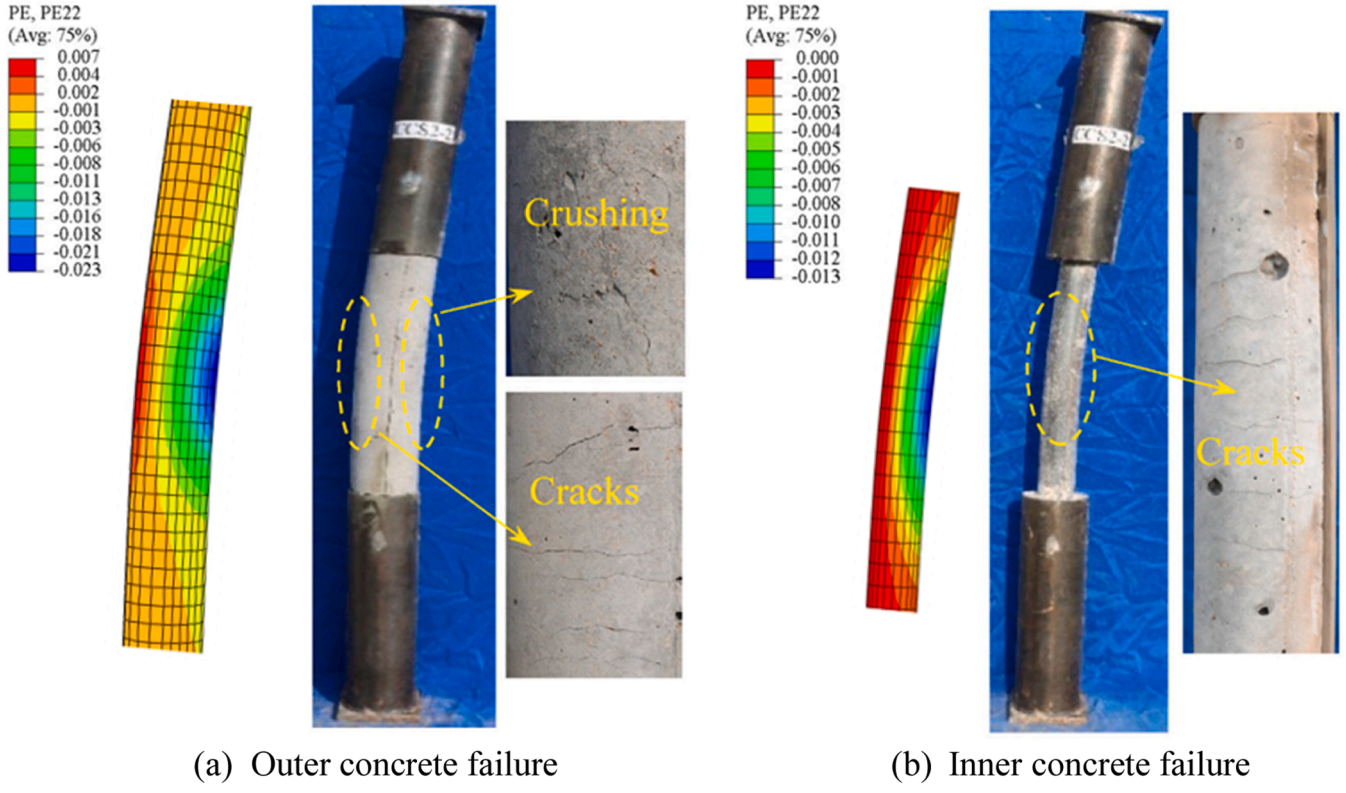

Fig. 12. Comparisons of the concrete failure mode between the FE model and experimental tests [36].

3.1. Slenderness (λ)

The slenderness (λ) is the most influential parameter governing the behaviour of slender CFDST columns. Fig. 17(a) presents the relationship between the axial compressive ultimate strength and slenderness for different width-to-thickness ratios (B_o/t_o), reflecting variations in cross-sectional size. It is evident that as the slenderness increases, the axial ultimate strength decreases significantly. This reduction is more pronounced at lower B_o/t_o ratios. To evaluate the effect of slenderness on normalised axial strength, Fig. 17(b) shows the corresponding trends for

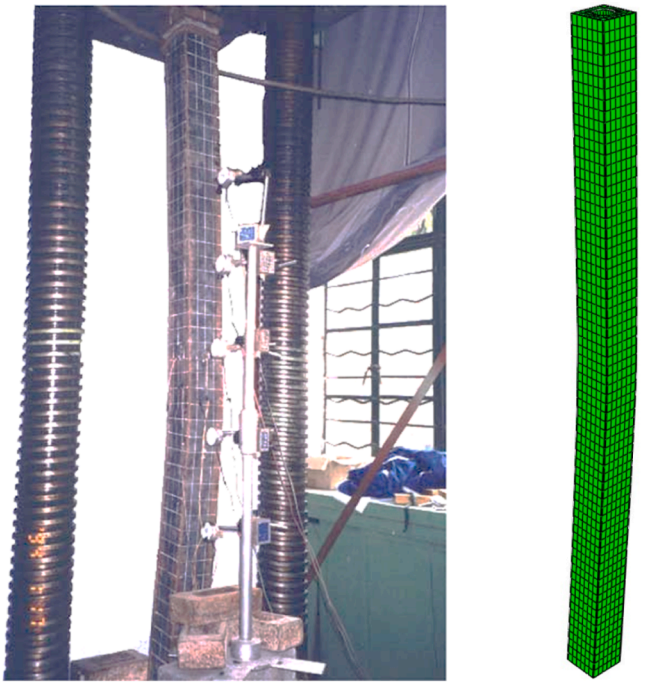

Fig. 13. Final deformed shape of slender column scbc4–1 [45].

three B_o/t_o ratios. Similar behaviour is observed across all three cases, indicating a consistent influence of λ on the normalised strength irrespective of cross-section slenderness.

Fig. 18(a) illustrates axial load *versus* mid-height lateral deflection curves for columns with $B_o = 200$ mm, over a range of slenderness values from 22 to 165. At lower slenderness values, the axial load drops sharply after reaching the peak load due to crushing of the infilled concrete. This failure mode is classified as inelastic buckling, typically seen in intermediate-length columns. As the slenderness increases, the post-peak response becomes more stable, with longer columns exhibiting higher lateral deflection capacity while maintaining their axial load-bearing ability. Furthermore, comparing columns S1, S17, and S33—each with approximately the same slenderness—demonstrates that these effects become more significant as B_o/t_o increases. This indicated that cross-sectional slenderness amplifies the influence of global slenderness on both strength and deformation characteristics.

3.2. Confinement and slenderness limits

Based on the FE modelling results, all pin-ended slender CFDST columns exhibited global (overall) buckling failure characterised by a half-sine wave deformation at mid-height. However, this buckling mode may occur either elastically or inelastically. To distinguish between intermediate-length and long CFDST columns, the relationship between axial load capacity $N_{ult,FE}$ and the ratio of $\varepsilon_h/\varepsilon_{lc}$ was examined. Here ε_{lc} and ε_h represent the longitudinal and hoop strains of the stainless steel tube in the compression zone at mid-height of each column, respectively. Fig. 18(b) shows this relationship for Group G1 with $B_o = 200$ mm. It is evident that for columns S10 to S14, the Poisson effect persists up to the ultimate load, indicating that lateral confinement is absent due to minimal transverse expansion of the concrete in the elastic range [59]. This behaviour confirms that these columns failed in an elastic buckling mode and are thus classified as long columns. In contrast, for columns S1 to S9, a clear confinement effect is observed near the ultimate load—indicated by $\varepsilon_h/\varepsilon_{lc} \geq 0.30$—due to lateral dilation from micro-cracking in the concrete. This suggests the presence of inelastic buckling, categorising these as intermediate-length columns.

Table 6 summarises the failure modes for Groups G1, G2, and G3, where EB and INB denote elastic and inelastic buckling failure, respectively. The results confirm that failure mode is primarily governed by the column's slenderness (λ). From the results, the slenderness limit (λ_r) that distinguishes intermediate-length from long columns is found to be approximately 100 across varying cross-sectional widths. For outer tube yield strength $f_{yo} = 530$ MPa, this corresponds to a non-dimensional slenderness limit of $\overline{\lambda}_r = 1.37$ (as per Eq. 15). A generalised expression for the slenderness limit of slender square CFDST columns may be proposed as $\lambda_r = 150/\sqrt{\frac{f_{yo}}{235}}$. Additionally, the plastic non-dimensional

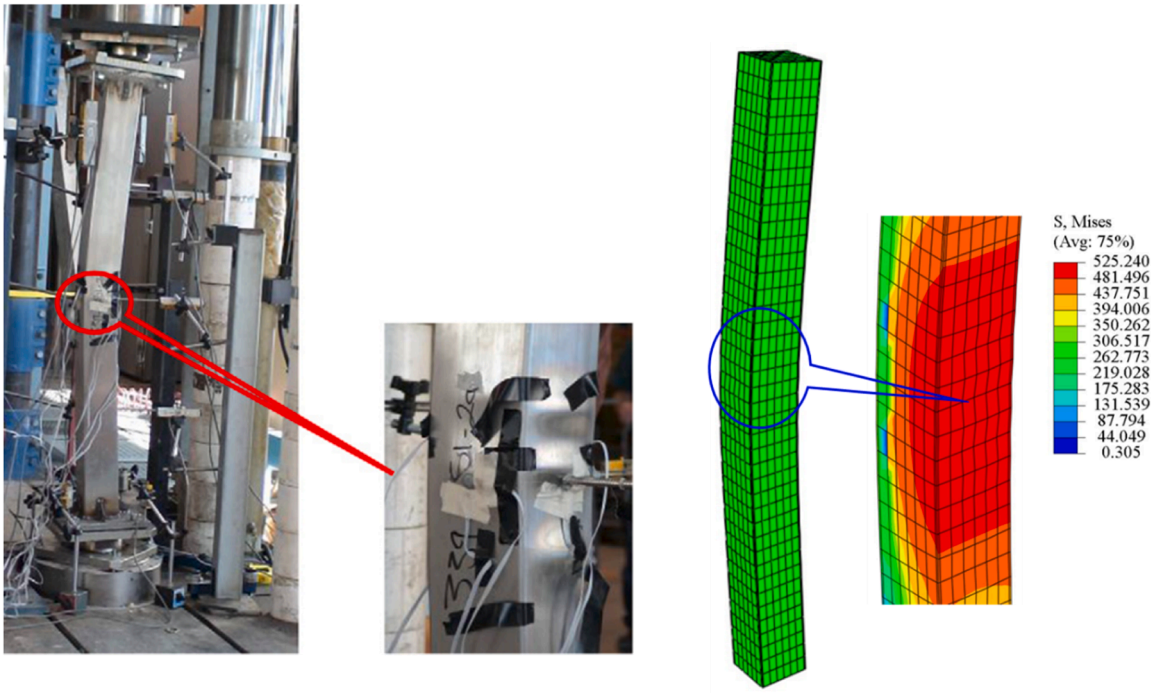

Fig. 14. Buckled shape of slender column S1–2a [46].

Table 3
Geometrical and material properties of square-square CFDST short columns [4].

Specimen	B_o (mm)	t_o (mm)	B_i (mm)	t_i (mm)	L (mm)	f_{yo} (MPa)	f_{yi} (MPa)	f_c' (MPa)	n	m
									Outer (Inner)	Outer (Inner)
LS100 × 3-NS40 × 4-C40	100.3	3.15	40.0	3.84	250	556	404	41.8	6 (3)	4 (4)
LS100 × 3-NS40 × 4-C40R	100.2	3.16	40.0	3.86	250	556	404	41.8	6 (3)	4 (4)
LS100 × 3-NS40 × 4-C80	100.2	3.13	40.0	3.87	250	556	404	81.6	6 (3)	4 (4)
LS100 × 3-NS40 × 4-C120	100.2	3.14	40.0	3.86	250	556	404	115.9	6 (3)	4 (4)
LS100 × 3-NS40 × 1.5-C40	100.3	3.18	40.4	1.42	250	556	324	41.8	6 (16)	4 (4)
LS100 × 3-NS40 × 1.5-C80	100.2	3.15	40.4	1.44	250	556	324	81.6	6 (16)	4 (4)
LS100 × 3-NS40 × 1.5-C120	100.2	3.15	40.4	1.44	250	556	324	115.9	6 (16)	4 (4)

Table 4
Comparisons between the FE model and experimental results for CFDST short columns [4].

Specimen	$N_{ult,Exp.}$ **(kN)**	$N_{ult,FE.}$ **(kN)**	$N_{ult,FE}/N_{ult,Exp.}$
LS100 × 3-NS40 × 4-C40	1420	1289	0.91
LS100 × 3-NS40 × 4-C80	1464	1518	1.04
LS100 × 3-NS40 × 4-C120	1706	1794	1.05
LS100 × 3-NS40 × 1.5-C40	1209	1140	0.94
LS100 × 3-NS40 × 1.5-C80	1323	1373	1.04
LS100 × 3-NS40 × 1.5-C120	1516	1641	1.08
Avg.			**1.01**
SD.			**0.068**

slenderness limit $\bar{\lambda}_o$ can be used to define the transition from short to intermediate-length columns. It is found that $\bar{\lambda}_o = 0.5$ is an appropriate threshold for identifying columns where global buckling has negligible influence on the ultimate strength. This corresponds to a slenderness limit of $\lambda_p = 37$, which can be generalised as $\lambda_p = 55/\sqrt{\frac{f_{yo}}{235}}$. These proposed limits provide a rational basis for classifying CFDST column behaviour under axial compression and offer a practical reference for design applications.

An additional means of differentiating between intermediate-length and long CFDST columns is through examining the stress distribution in the sandwiched concrete. Fig. 19 illustrates the axial stress distribution of the infilled concrete at $N_{utl,FE}$ for both intermediate-length and long CFDST columns—specifically, columns S7 and S16, respectively—at the mid-height section. In case of the intermediate-length column (S7), shown in Fig. 19(a), compressive stresses dominate across the entire cross-section, indicating a uniform compressive response. In contrast, Fig. 19(b) reveals that for the long column (S16), the stress distribution varies significantly across the section, exhibiting both tensile and compressive regions. This variation is attributed to the overall buckling behaviour, which induces bending and consequently results in a non-uniform stress state across the concrete core.

3.3. Effect of B_o/t_o ratio

Fig. 20 illustrates the relationship between B_o/t_o and the normalised strength ($N_{ult,FE}/N_{ult,pl,Rd}$) for various slenderness ratios, considering both intermediate-length and long CFDST columns. An increase in B_o/t_o from 25 to 37.5 has no significant effect on the normalised strength of intermediate-length columns. In contrast, for long columns, this increase results in only a slight effect on the normalised strength. With regard to the influence of B_o/t_o on the normalised strength–lateral deflection response, as depicted in Fig. 21, increasing this ratio from 25 to 37.5 had negligible impact on the strength–deflection behaviour at the mid-height section for both intermediate-length and long columns. This observation is attributed to the governing failure mode of these columns—global buckling—which is primarily influenced by the slenderness (λ). Therefore, employing higher B_o/t_o ratios is advantageous in design, as it contributes to material efficiency by reducing the required amount of steel without compromising structural performance.

3.4. Effect of concrete grade

In this section, two concrete grades—40 MPa and 80 MPa—were examined to investigate the influence of concrete compressive strength on the structural behaviour of intermediate-length and long CFDST columns. As illustrated in Fig. 22(a), increasing the concrete strength from 40 MPa to 80 MPa resulted in an increase in ultimate axial strength by approximately 22 %, 21 %, 18 %, and 17 % for intermediate-length columns with slenderness ratios λ= 41,60 and 78, respectively. For long columns, the enhancement in concrete strength similarly increased

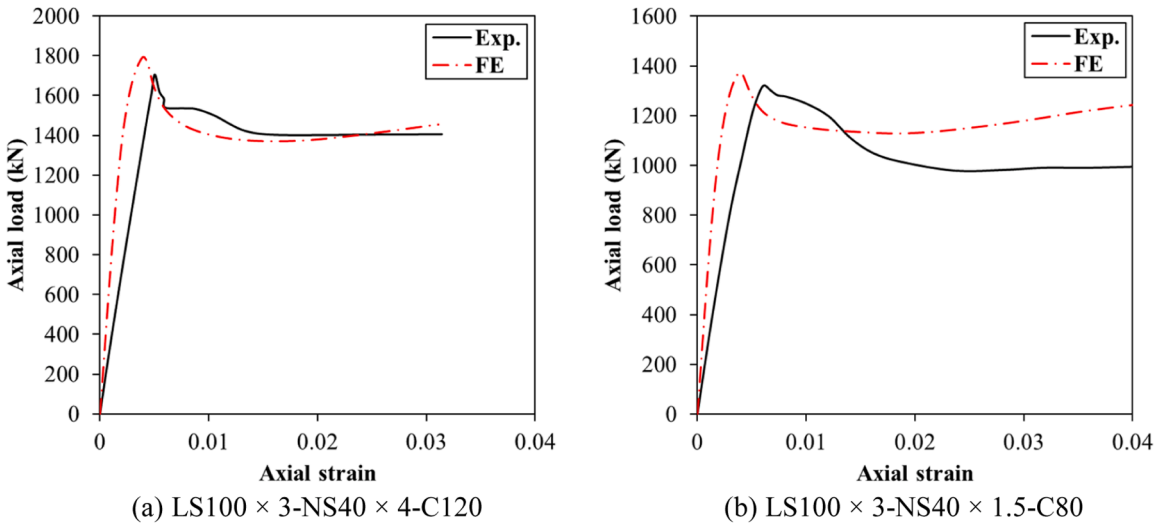

Fig. 15. Axial load *versus* axial strain for short specimens [4].

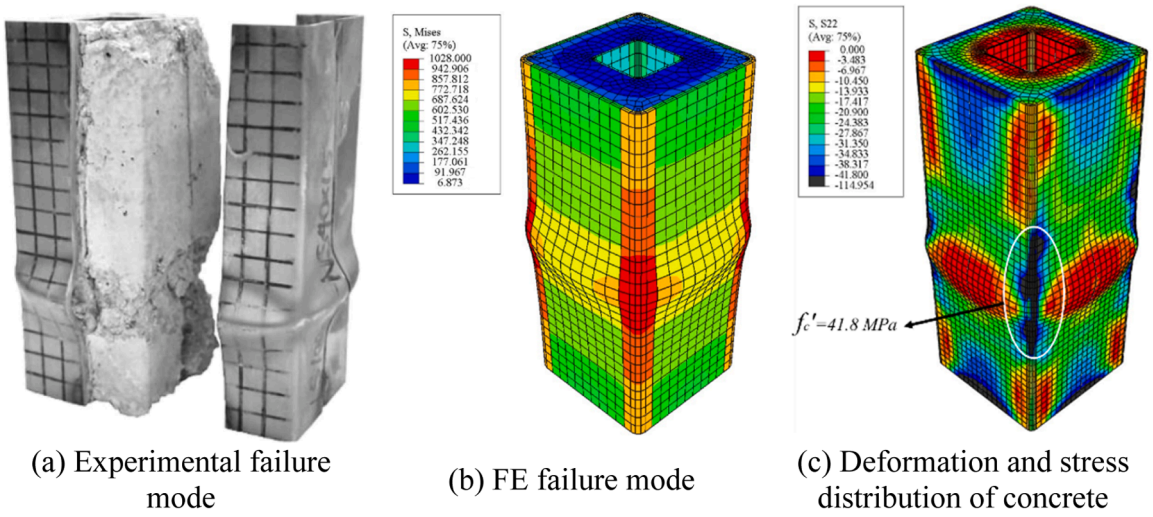

Fig. 16. Experimental and numerical failure modes for specimen LS100 × 3-NS40 × 1.5-C40 [4].

Table 5
Range of investigated parameters of slender CFDST columns.

Parameter	λ	B_o/t_o	f_c' (MPa)	$\bar{\chi}$
value/range	22 ~ 175	25 ~ 66.67	40, 80	0.33 ~ 0.71

the ultimate axial strength by around 17 %, irrespective of the slenderness ratio.

However, as shown in Fig. 22(b), increasing the concrete strength had negligible impact on the normalised strength. The effect of concrete strength on axial load-lateral deflection behaviour is illustrated in Fig. 23. A comparison between intermediate-length columns S3, S5, S7, and S9 (with f_c'=40 MPa) and their geometrically identical counterparts S49, S50, S51, and S52 (with f_c'=80 MPa) exhibited similar trends throughout the loading process, with differences observed only in the load-bearing capacities, which increased due to the use of higher strength concrete, as depicted in Fig. 23(a). This behaviour was consistent in long columns, as shown in Fig. 23(b).

Fig. 24 presents the influence of concrete strength on the normalised strength-lateral deflection response. For intermediate-length columns (see Fig. 24(a)), specimens S3 and S49, which share the same slenderness ratio (λ=41) but differ in concrete strength, showed a notable improvement in post-peak performance with the use of higher strength concrete. A similar effect is observed when comparing columns S5 and S50 (λ=60). Conversely, for long columns, the influence of increasing f_c' from 40 MPa to 80 MPa was marginal, as evidenced by the comparison between S11 and S53, and between S13 and S54 in Fig. 22 (b).

Furthermore, as presented in Table A, increasing the concrete strength from 40 MPa to 80 MPa lead to an average increase in the strength-to-weight (*STW*) ratio of approximately 20 % and 17 % for intermediate-length and long columns, respectively. This improvement is attributed to the enhanced load-carrying capacity of the section due to the use of higher strength concrete, while the self-weight of the columns remains constant.

3.5. Effect of hollow ratio

Fig. 25 illustrates the effect of the hollow ratio on both the ultimate and normalised axial strengths. Three different inner tube widths—60 mm, 100 mm, and 130 mm—were considered, corresponding to hollow ratios of 0.33, 0.54, and 0.71, respectively. For

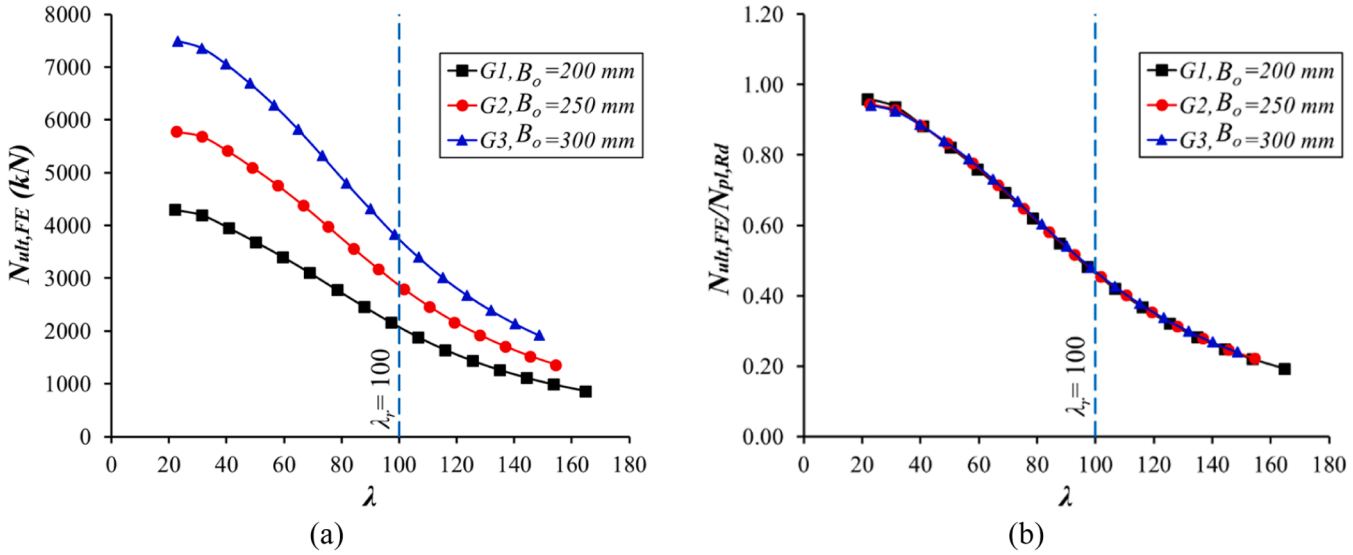

Fig. 17. Effect of λ on (a) the ultimate strength and (b) the normalised ultimate strength of slender square CFDST columns.

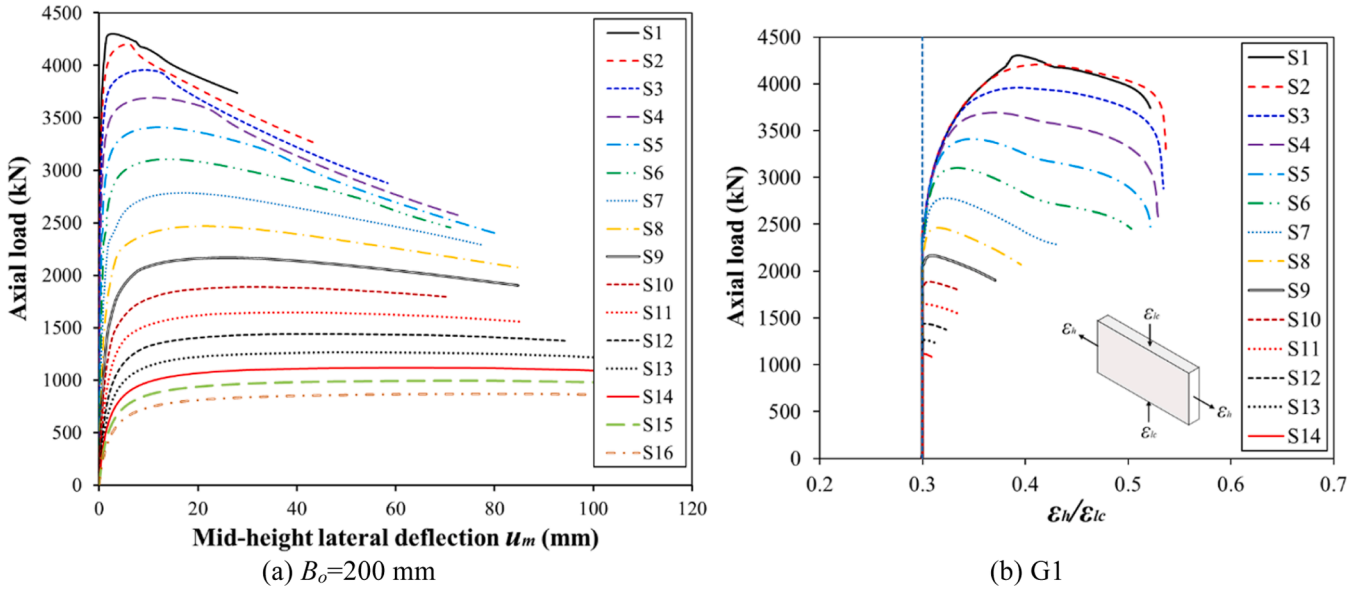

Fig. 18. Axial capacity *versus* (a) mid-height deflection and (b) $\varepsilon_h/\varepsilon_{lc}$.

Table 6
Failure modes of slender square CFDST columns (for various λ and B_o).

G1	λ	22	41	60	78	97	107	125	144	165
	Failure mode	INB	INB	INB	INB	INB	EB	EB	EB	EB
G2	λ	23	40	58	75	93	102	119	137	154
	Failure mode	INB	INB	INB	INB	INB	EB	EB	EB	EB
G3	λ	23	40	57	73	98	107	123	140	149
	Failure mode	INB	INB	INB	INB	INB	EB	EB	EB	EB

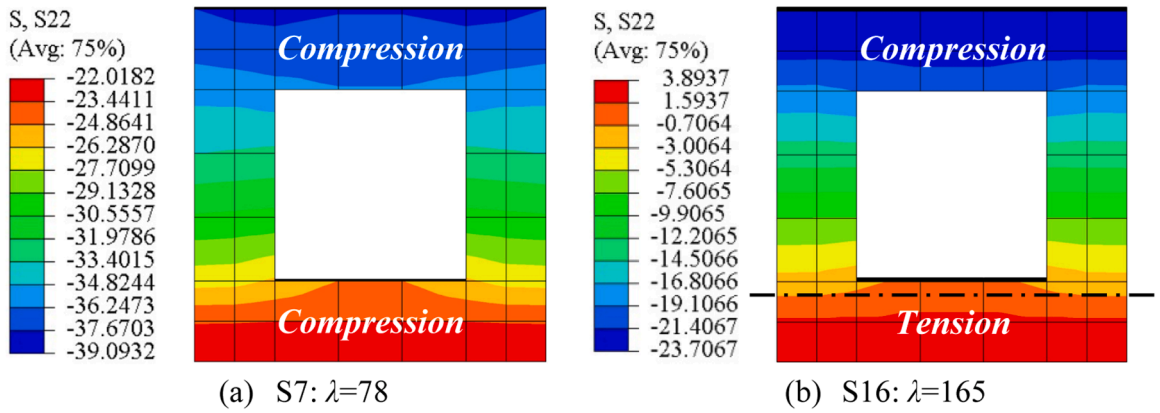

Fig. 19. Axial stress distribution in the infilled concrete at $N_{ult,FE}$ for (a) intermediate-length and (b) long CFDST columns.

intermediate-length CFDST columns, increasing the hollow ratio from 0.33 to 0.71 resulted in a minor reduction in ultimate strength of approximately 3 %. Conversely, for long CFDST columns, the same increase in hollow ratio led to a 4.5 % increase in ultimate strength. As shown in Fig. 25(b), the effect of the hollow ratio on normalised axial strength was negligible for intermediate-length columns. However, for long columns, an average increase of approximately 9 % in normalised strength was observed. These findings indicate that the section hollow ratio has a marginal influence on the behaviour of slender square CFDST columns, particularly for those of intermediate length. Additionally, as indicated in Table A, increasing the hollow ratio from 0.33 to 0.71 resulted in an average increase in the strength-to-weight (*STW*) ratio of 16 % for intermediate-length columns and 24 % for long columns. This improvement is attributed to the significant reduction in the self-weight of the columns at higher hollow ratios.

3.6. Contact pressure mechanism

To clarify the underlying mechanism of the confinement behaviour in slender square CFDST columns with an outer stainless steel skin, a contact pressure analysis was conducted. This analysis aimed to investigate the interaction between the outer tube and the confined concrete by examining the contact pressure (p) at critical locations. Four slender columns were analysed—two intermediate-length columns and two long columns. Two specific locations on the mid-height cross-section, denoted as points "a" (compression corner) and "b" (tension corner), were selected for detailed assessment, as illustrated in Fig. 26.

The evolution of contact pressure with respect to lateral mid-height

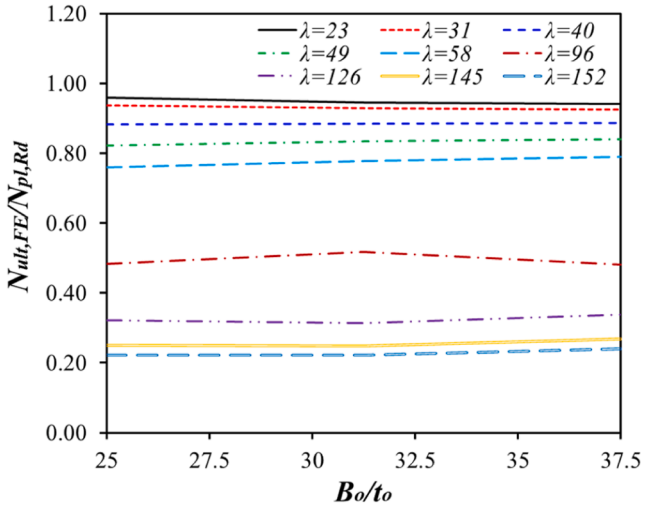

Fig. 20. Influence of B_o/t_o ratio on the normalized strength at various slenderness ratios.

deflection is presented on the left-hand side (LHS) of Fig. 27. A comparison of the four columns reveals that, as the slenderness (λ) increased, the contact pressure at both compression and tension corners decreased. Furthermore, in intermediate-length columns, the contact pressure at the tension corner (point "b") was consistently greater than that at the compression corner (point "a"). For long columns, the contact pressures at both corners increased in a more uniform manner, although their peak values remained substantially lower than those observed in intermediate-length columns. Additionally, an increase in λ significantly delayed the development of the contact stress, as evident in Fig. 27(a) and Fig. 27(b) (LHS).

On the right-hand side (RHS) of Fig. 27, the distribution of contact pressure at the mid-height section is shown at the point of maximum contact pressure. It is observed that the contact pressure reached its maximum at the corners of the section and reduced to zero at the midpoint of each side of the cross-section. Moreover, consistent with previous observations, the contact pressure at the tension corners (point "b") exceeded that at the compression corners (point "a"). These trends are observed in both intermediate-length and long columns, although long columns with higher slenderness ratios exhibited notably lower overall contact pressures.

4. Evolution of material behaviour and failure mechanism

The numerical results were further analysed to provide a detailed understanding of the evolution of the mechanical behaviour of materials at various loading stages for intermediate-length (S3) and long (S12) square CFDST columns, with slenderness ratios (λ) of 41 and 125, respectively. The responses of both the steel tubes and the concrete were investigated in terms of longitudinal stresses, the progression of plasticity, and the development of concrete damage and strain. The stainless steel exhibited a rounded stress–strain response, while the confined concrete behaviour was modelled using the Concrete Damaged Plasticity (CDP) approach. The behaviour of each material from the onset of loading to ultimate failure is discussed as follows, with the concrete compressive damage illustrated along the half-length of the columns for clarity.

4.1. Initial elastic stage

At the onset of loading, both the steel tubes and the concrete core exhibited linear elastic behaviour in the intermediate-length and long columns. To illustrate the elastic stage, the equivalent plastic strain and concrete compressive damage at 50 % of the ultimate load (N_{ult}) are presented for the intermediate-length column S3, as shown in Fig. 28. During this stage, axial deformation was primarily resisted by both materials without significant inelastic effects, and no concrete damage or plastic strain was observed. The longitudinal stresses were uniformly distributed across the cross-section, indicating that the load was effectively shared among the three components: the outer tube, inner tube, and infilled concrete.

In the case of the long composite column S12, Fig. 29 presents the equivalent plastic strain and concrete compressive damage at 50 % of N_{ult}. Similar behaviour to that of column S3 is observed. However, lower values of longitudinal stress were recorded across the cross-section, reflecting the reduced ultimate load capacity of this column due to its lower global stability. Additionally, a non-uniform stress distribution was observed, particularly in the outer tube.

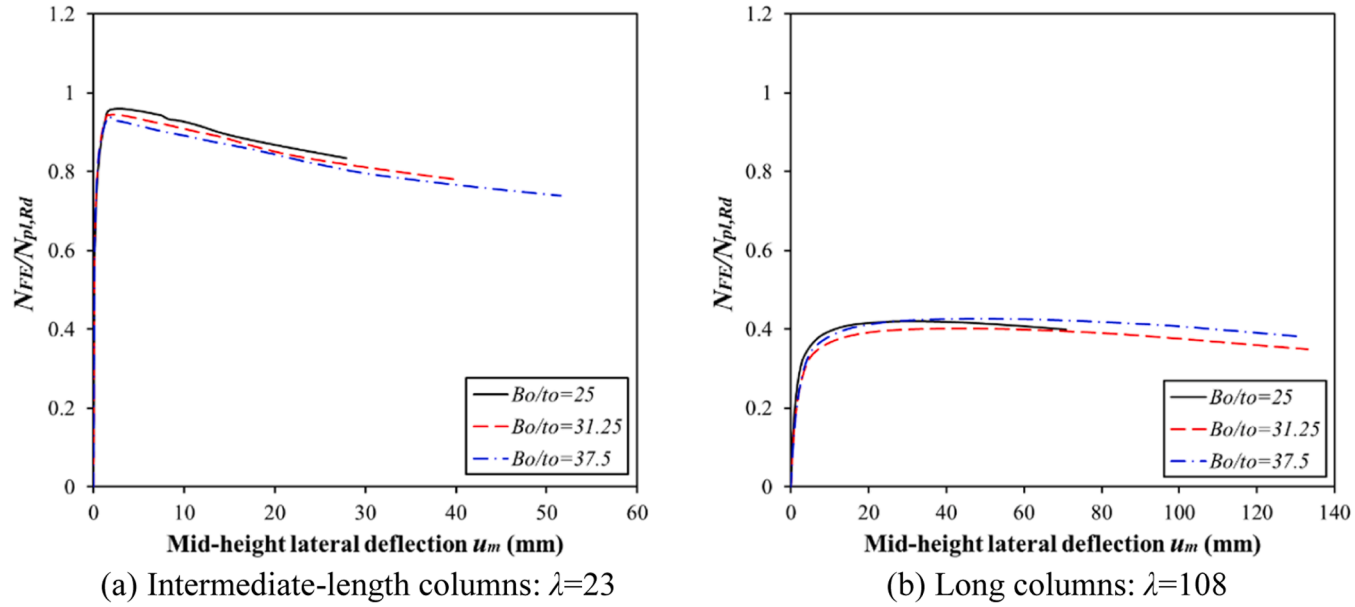

Fig. 21. Influence of B_o/t_o ratio on the normalized strength-lateral deflection curves.

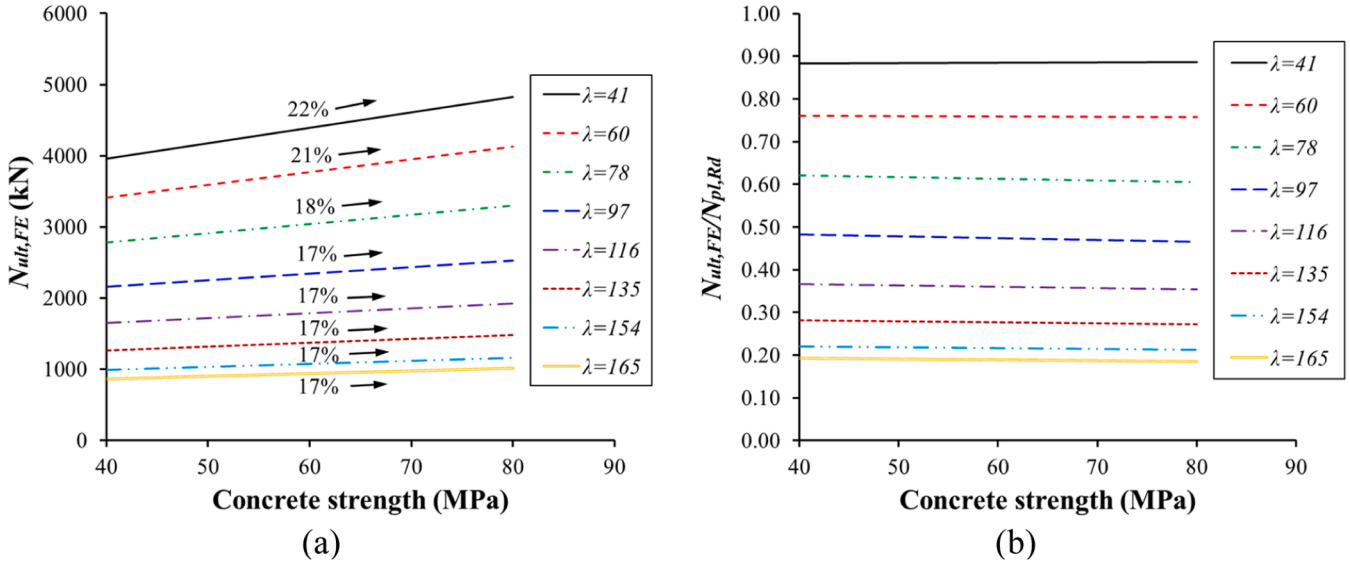

Fig. 22. Effect of concrete strength on: (a) ultimate and (b) normalized strengths.

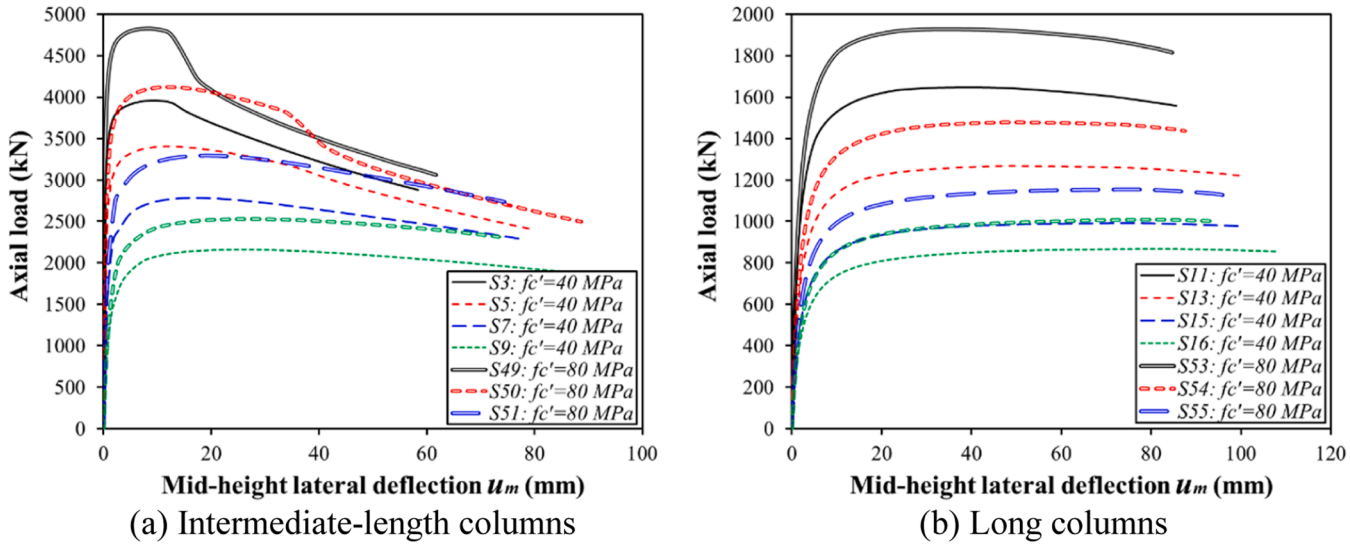

Fig. 23. Effect of concrete strength on the axial load-lateral deflection responses.

4.2. Onset of plasticity and confinement effect

As the axial load increased to 75 % of the ultimate load (N_{ult}), plasticity first developed in the inner tube and the concrete core of the intermediate-length column S3. Subsequently, the outer tube began to exhibit plastic behaviour, primarily on the compression side, where stress concentration occurred due to the bending effects associated with global buckling. The equivalent plastic strain (PEEQ) contours indicated early yielding in this region, consistent with the nonlinear stress–strain response described by the Ramberg–Osgood model. At the same time, lateral dilation of the concrete core activated the confinement effect provided by the surrounding steel tubes, contributing to enhanced axial strength and delaying the onset of concrete compressive damage, as illustrated in Fig. 30. Notably, the longitudinal stresses remained uniformly distributed across the cross-section at this stage.

In contrast, at 75 % of N_{ult}, no plasticity was observed in the cross-section of the long column S12, as shown in Fig. 31(a). However, a noticeable non-uniformity in longitudinal stress distribution was identified at this loading stage, as presented in Fig. 31(b). Furthermore, there was no evidence of concrete compressive damage at this point, as clearly indicated in Fig. 31(c).

4.3. Progressive plasticity development and peak load

It is observed in Fig. 32(a)that with continued application of axial load up to the peak (ultimate) load, plasticity progressively spread across the cross-section of the intermediate-length column S3, with higher values concentrated on the compression side compared to the tension side—particularly near mid-height, where bending deformation associated with global buckling began to develop. Additionally, the axial stresses in the outer steel tube became non-uniform, with elevated values on the compression side, as illustrated in Fig. 32(b). The equivalent plastic strain increased steadily, indicating ongoing yielding in the steel tube, while the concrete core experienced rising compressive stresses. At this stage, the confinement effect became more prominent, enhancing both the ductility and load-bearing capacity of the column.

The CDP concrete model facilitated tracking the development of damage. Fig. 32(c) shows the distribution of compressive damage along

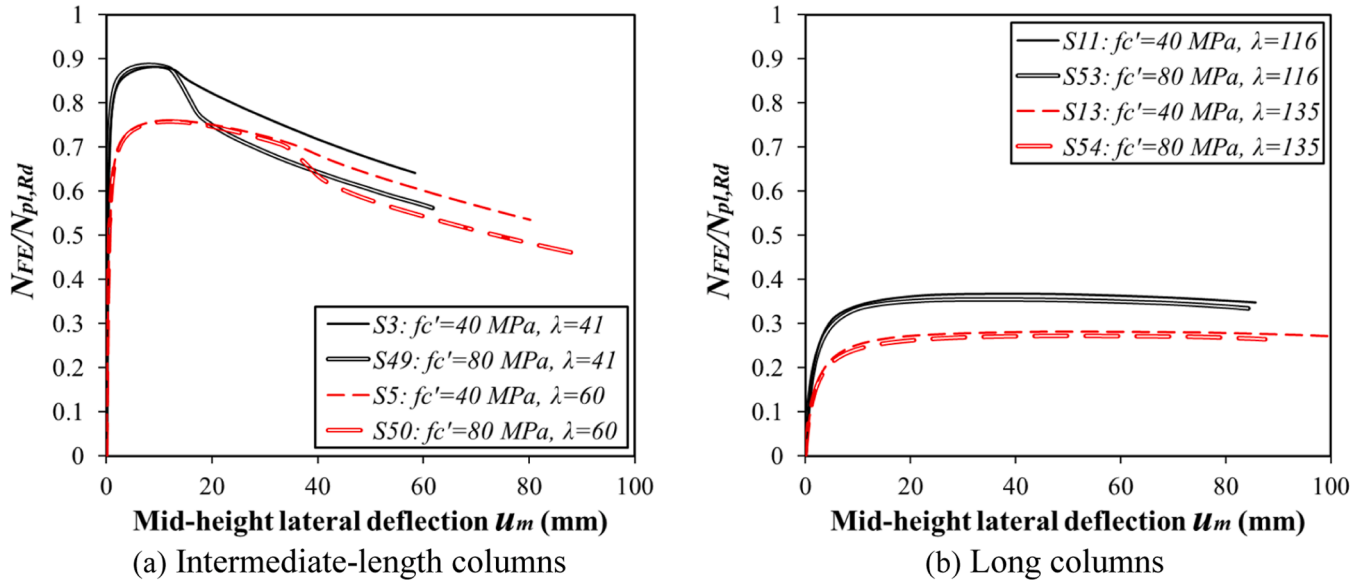

Fig. 24. Effect of concrete strength on the normalized strength-lateral deflection responses.

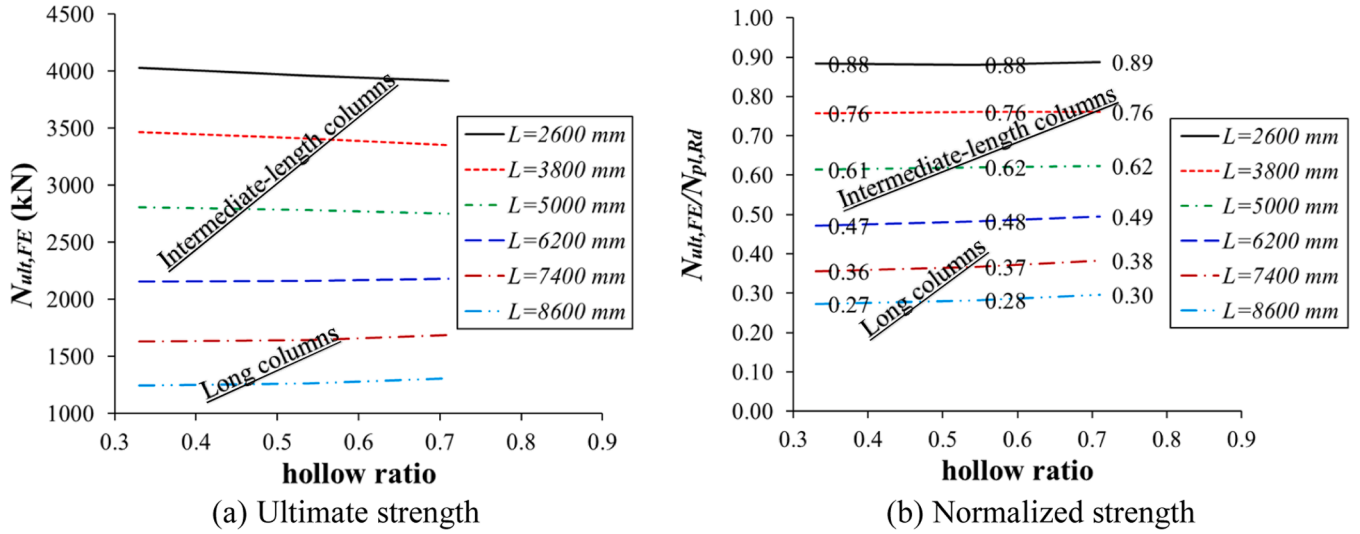

Fig. 25. Effect of hollow ratio on the ultimate and normalized strengths of CFDST slender columns.

half the column length. Damage initiated on the compression side—especially at mid-height where the maximum lateral displacement occurred—and concrete crushing began in these regions. With further loading, the damage propagated, contributing to a gradual reduction in stiffness. In contrast, for the long column S12, the equivalent plastic strain had only just initiated on the compression side of the concrete core, as shown in Fig. 33(a). No plasticity was observed on the tension side, unlike in column S3. With respect to concrete compressive damage and longitudinal stress distribution (Fig. 33(c)), no significant changes were observed from the previous loading stage, apart from an increase in the magnitude of longitudinal stresses, as depicted in Fig. 33(b).

4.4. Post-peak behaviour and failure modes

The numerical simulations consistently demonstrated that global buckling was the primary failure mode for the investigated square CFDST slender columns. Neither local buckling nor premature material failure dominated, owing to the beneficial confinement effect provided by the steel tubes and the relatively high slenderness ratios considered in the study. While the progressive development of plasticity and concrete damage significantly influenced the post-peak behaviour, it did not alter the global buckling failure pattern. The material response was examined in the post-peak stage at a compressive strain equal to 1.5 times the yield strain ($1.5\varepsilon_y$ = 6975 με). The post-peak behaviour showed a gradual decline in axial load, primarily driven by the global buckling deformation, which remained the dominant failure mechanism across all the studied columns.

As shown in Fig. 34(a), for the intermediate-length column S3, the equivalent plastic strain increased markedly as the steel tubes fully yielded on the compression side. However, the strain distribution across the cross-section was clearly non-uniform, with the maximum values concentrated on the compressed region of the concrete core. This indicates a high level of confinement achieved in the sandwiched concrete. Additionally, the axial stresses in the steel tubes exceeded the material's yield stress, as depicted in Fig. 34(b). Concrete compressive damage also increased significantly due to the global buckling-induced deformation, as illustrated in Fig. 34(c). In the case of the long column S12 (Fig. 35), the equivalent plastic strain also increased considerably compared to the

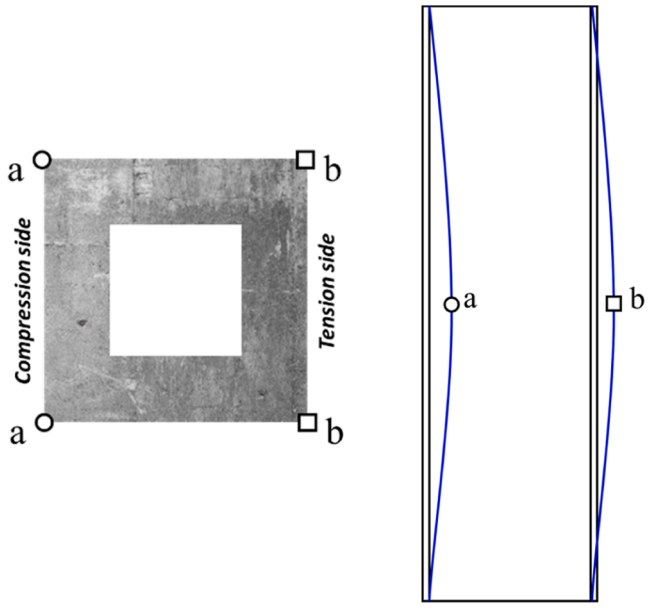

Fig. 26. Locations of maximum contact pressure on the compression and tension sides of sandwiched concrete.

previous loading stage, with the maximum values observed on the compression side of the outer steel tube. This highlights the lower confinement effect present in long columns relative to intermediate-length ones. Furthermore, concrete compressive damage began to emerge at this stage, with Fig. 35(c) showing that global instability directly influenced the onset and progression of concrete damage.

4.5. Concrete damage propagation

To gain a deeper understanding of the mechanism behind concrete compressive damage, an analysis was conducted to further explore this critical aspect. As illustrated in Fig. 36(a), the relationship between concrete damage on the compression side and concrete longitudinal strain was plotted for the intermediate-length column S3. It is observed that concrete damage initiated near the peak load (N_{ult}), confirming that concrete damage due to axial compressive stresses significantly influences the overall buckling failure in intermediate-length CFDST columns. Furthermore, as loading progressed, the damage increased markedly until reaching a strain of 1 % (point A). Beyond this, the rate of increase in concrete damage slowed until it attained its maximum value at point B.

To illustrate the development of concrete compressive damage distribution, three points were considered: the peak load, point A, and point B, as shown in Fig. 36(b). At peak load, concrete damage was minimal and fairly evenly distributed along the column's mid-height. As axial strain increased, a slight increase in damage was observed along the entire length, except for a small region around mid-height where the damage rose considerably—likely due to initial micro-cracking in the concrete. By the end of loading (point B), damage had significantly increased over a large portion of the column. Fig. 36(c) shows that concrete damage gradually increased with lateral deflection up to approximately 12 mm, after which a sudden rise in damage was evident during the post-peak loading stage. This confirms that concrete damage was primarily driven by global buckling failure and had a pronounced effect on the stability of slender square CFDST columns.

In contrast, for the long column S12, concrete damage was noted to commence only after the peak load, as indicated in Fig. 37(a). Compared with intermediate-length columns, the concrete damage in long columns was less severe. Fig. 37(b) presents the distribution of concrete damage at point B, where compressive damage was minimal and confined to a small region around mid-height. Fig. 37(c) illustrates the propagation of concrete damage alongside mid-height lateral deflection, showing a close correlation with damage progression plotted against concrete compressive strain in Fig. 37(a).

5. Current design methods

This section evaluates the applicability of existing design procedures to the slender CFDST columns investigated in this study. Design models from EC4 [39], AISC 360–16 [38], and AS/NZS 2327 [40] are assessed for their suitability in predicting the behaviour of square- slender square CFDST columns. To account for the susceptibility of thin-walled sections to local buckling, the effective cross-sectional area of the outer tube ($A_{so,eff}$) is considered in the estimation of ultimate column strength, in accordance with EC3 Part 1–1 [41].

5.1. EC4

For slender square CFDST columns, the design approach specified in EC4 Part 1–1 [39] for conventional CFST columns is extended. According to EC4, the ultimate axial strength $N_{ult,EC4}$ of a composite slender column is given by:

$$N_{ult,EC4} = \chi_{EC3} N_{pl,Rd} \tag{20}$$

Here, χ_{EC3} is the buckling reduction factor based on the EC3 buckling curves [41], originally proposed by Ayrton and Perry [60], and is calculated as:

$$\chi_{EC3} = \frac{1}{\phi + \sqrt{\phi^2 - \bar{\lambda}^2}} \quad \leq 1.0 \tag{21}$$

where ϕ is defined as:

$$\phi = 0.5\left[1 + \alpha(\bar{\lambda} - 0.4) + \bar{\lambda}^2\right] \tag{22}$$

The imperfection factor α is taken as 0.49 for cold-formed hollow stainless steel sections, as specified in EC3 [41]. The non-dimensional slenderness $\bar{\lambda}$ is calculated using Eq. (15), and the plastic resistance $N_{pl,Rd}$ is determined from Eq. (16).

5.2. AISC 360–16

Modifications are made to the design equations in AISC 360–16 [38] to account for the presence of the inner steel tube, which effectively replaces the longitudinal and transverse reinforcement in traditional CFST columns. The ultimate axial strength $N_{ult,AISC}$ of slender square CFDST columns is given by:

$$N_{ult,AISC} = \begin{cases} N_{pl,AISC}\left[0.658^{\frac{N_{pl,AISC}}{N_{cr,AISC}}}\right] & \frac{N_{pl,AISC}}{N_{cr,AISC}} \leq 2.25 \\ 0.877 N_{cr,AISC} & \frac{N_{pl,AISC}}{N_{cr,AISC}} > 2.25 \end{cases} \tag{23}$$

where $N_{pl,AISC}$ is the section plastic ultimate strength and is calculated as:

$$N_{pl,AISC} = A_{so,eff} f_{yo} + 0.85 A_{sc} f_c' + A_{si} f_{yi} \tag{24}$$

$N_{cr,AISC}$ is the elastic critical buckling load and is determined as:

$$N_{cr,AISC} = \frac{\pi^2 (EI)_{eff,AISC}}{L_e^2} \tag{25}$$

The effective flexural stiffness $EI_{eff,AISC}$ is defined as:

$$(EI)_{eff,AISC} = E_{so} I_{so} + E_{si} I_{si} + C_3 E_{sc} I_{sc} \tag{26}$$

where C_3, the coefficient of concrete effective rigidity in filled composite

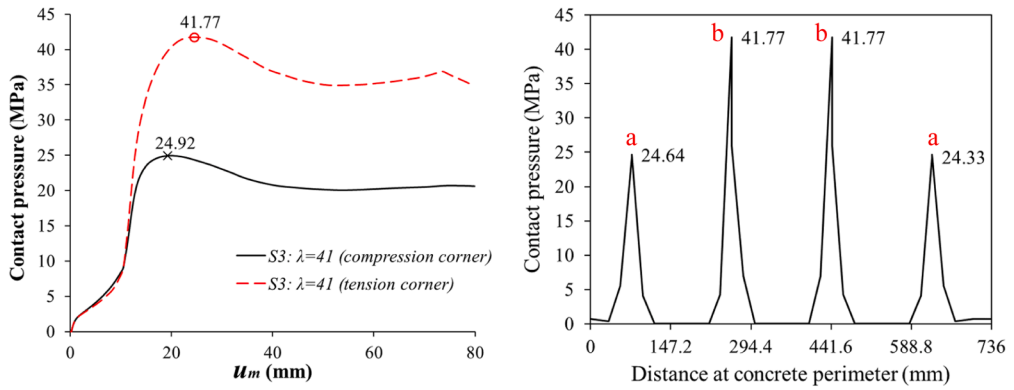

(a) S3: λ=41 (Intermediate-length column)

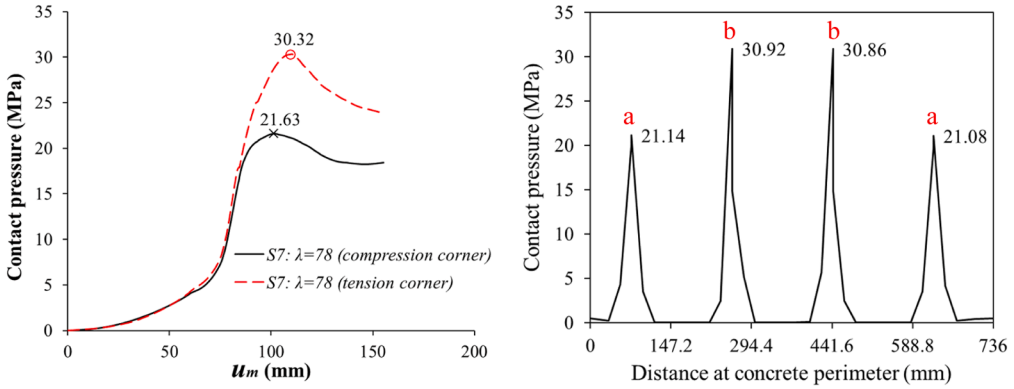

(b) S7: λ=78 (Intermediate-length column)

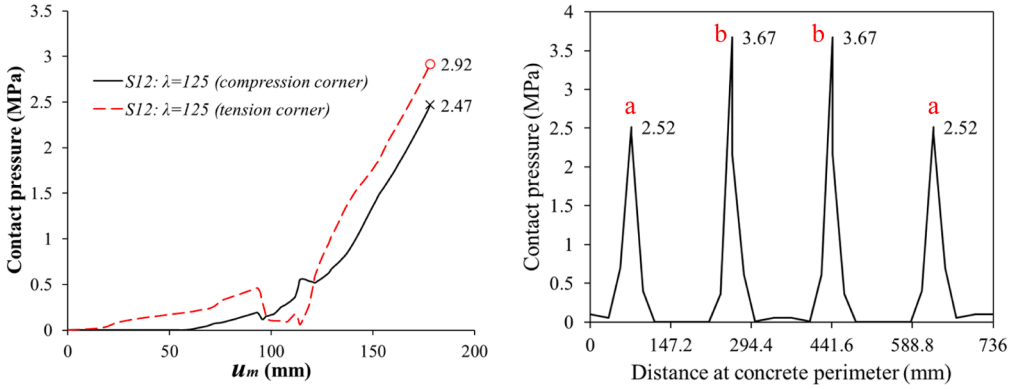

(c) S12: λ=125 (long column)

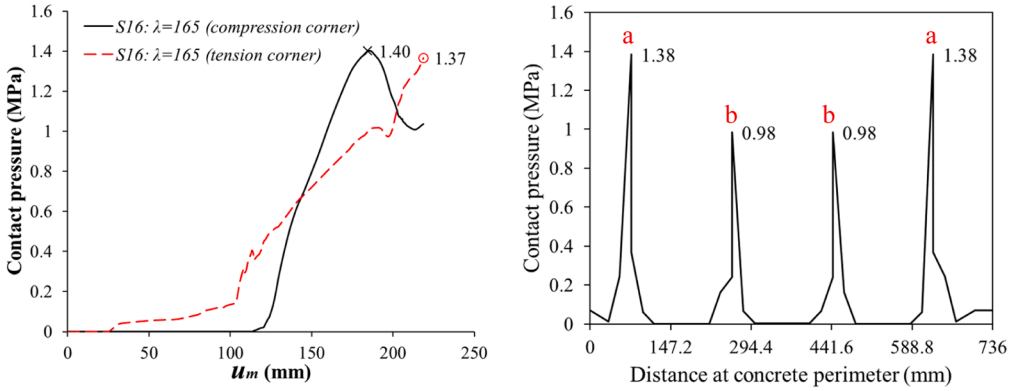

(d) S16: λ=165 (long column)

Fig. 27. Relationships of contact pressure *versus* mid-height lateral deflection and the perimeter of the concrete.

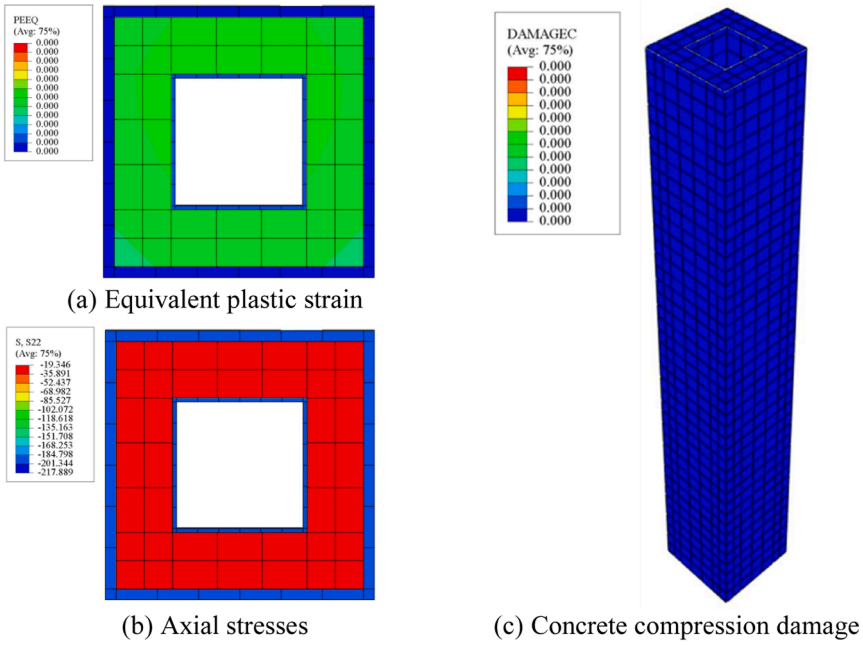

Fig. 28. Equivalent plastic strain, axial stresses, and concrete compression damage at the elastic stage of loading for intermediate-length column S3.

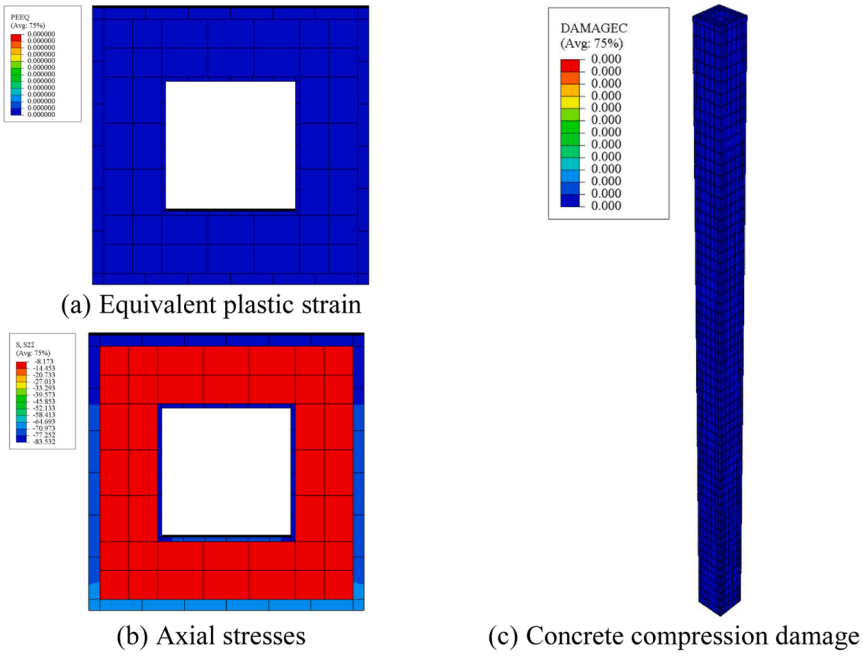

Fig. 29. Equivalent plastic strain, axial stresses, and concrete compression damage at the elastic stage of loading for long column S12.

compression members, is determined using Eq. (27):

$$C_3 = 0.45 + 3\left(\frac{A_{so} + A_{si}}{A_{so} + A_{si} + A_{sc}}\right) \leq 0.9 \tag{27}$$

5.3. AS/NZS 2327

The AS/NZS 2327 [40] specification, originally developed for rectangular CFST columns, is adapted for slender CFDST columns in this study. The ultimate axial strength $N_{ult,AS}$ is calculated as:

$$N_{ult,AS} = \chi_{AS} N_{pl,Rd} \tag{28}$$

The reduction factor χ_{AS} is determined as:

$$\chi_{AS} = \xi\left[1 - \sqrt{1 - (90/\xi\lambda)^2}\right] \leq 1 \tag{29}$$

with

$$\xi = \frac{(\lambda/90)^2 + 1 + \eta}{2(\lambda/90)^2} \tag{30}$$

and

$$\lambda = \lambda_\eta + \alpha_a \alpha_b \tag{31}$$

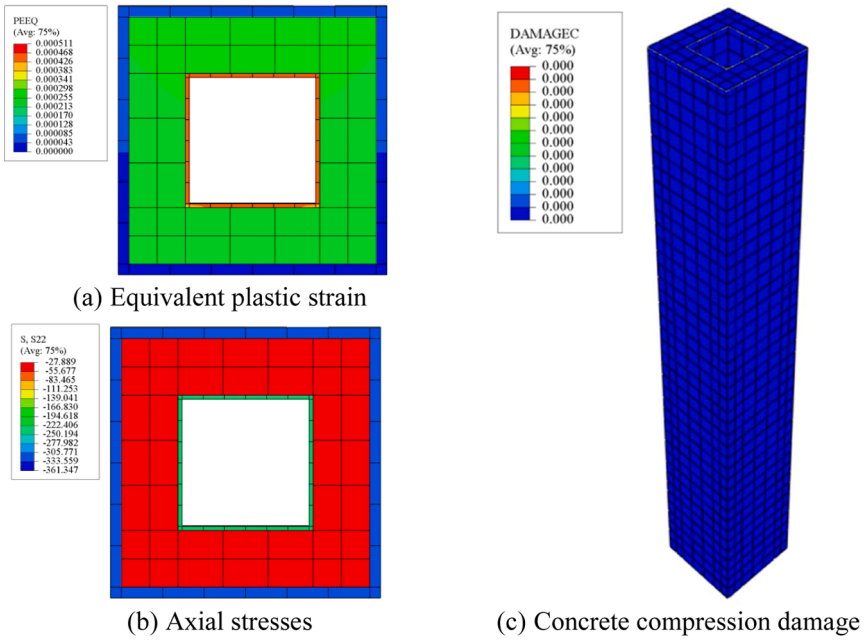

Fig. 30. Equivalent plastic strain, axial stresses, and concrete compression damage at the beginning of plastic stage of loading for intermediate-length column S3.

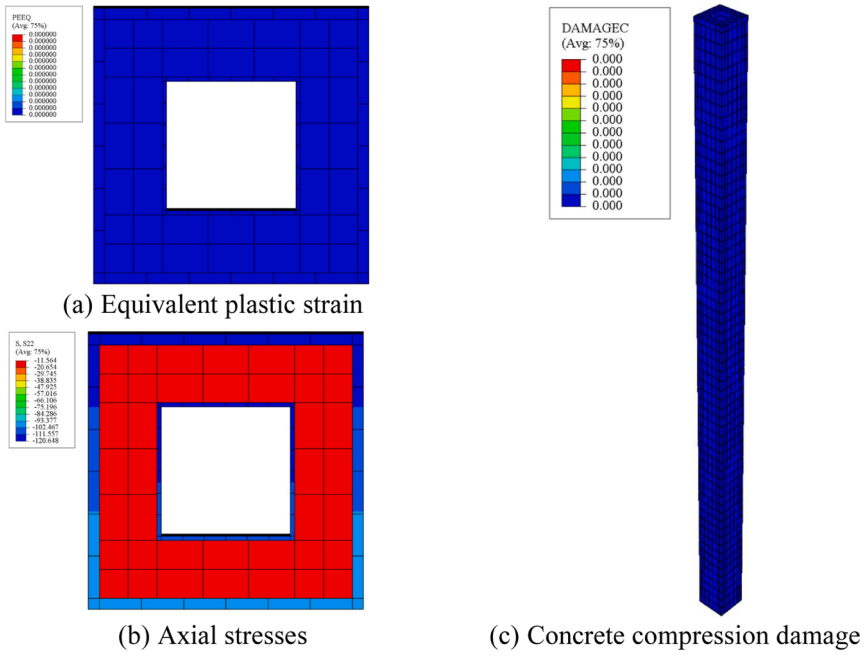

Fig. 31. Equivalent plastic strain, axial stresses, and concrete compression damage at the beginning of plastic stage of loading for long column S13.

$$\lambda_\eta = 90\lambda_r' \tag{32}$$

The relative slenderness λ_r' is calculated as:

$$\lambda_r' = \sqrt{\frac{N_{pl.Rd}}{\left(\frac{\pi^2 EI_{eff.AS}}{L_e^2}\right)}} \tag{33}$$

where the effective flexural stiffness is:

$$EI_{eff.AS} = E_{so}I_{so} + E_{si}I_{si} + E_{sc}I_{sc} \tag{34}$$

The parameter η is:

$$\eta = 0.00326(\lambda - 13.5) \geq 0 \tag{35}$$

The correction factors α_a and α_b are:

$$\alpha_a = \frac{2100(\lambda_\eta - 13.5)}{\lambda_\eta^2 - 15.3\lambda_\eta + 2050} \text{ and } \alpha_b = \begin{cases} 0 if \frac{A_{so.eff}}{A_{so}} < 1 \\ 1 if \frac{A_{so.eff}}{A_{so}} = 1 \end{cases} \tag{36}$$

5.4. Comparison of the design methods

This section compares the predicted ultimate strengths from the

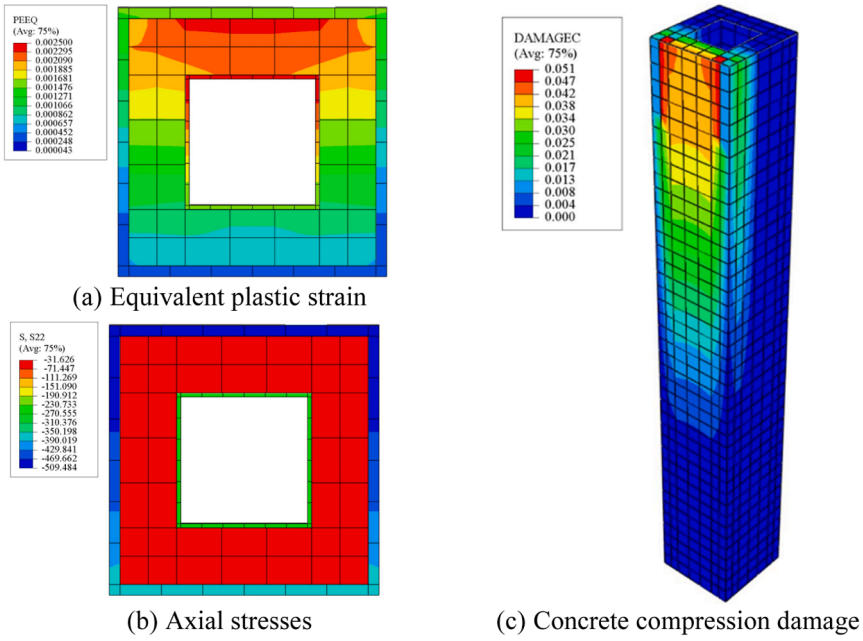

Fig. 32. Equivalent plastic strain, axial stresses, and concrete compression damage at the peak load stage for intermediate-length column S3.

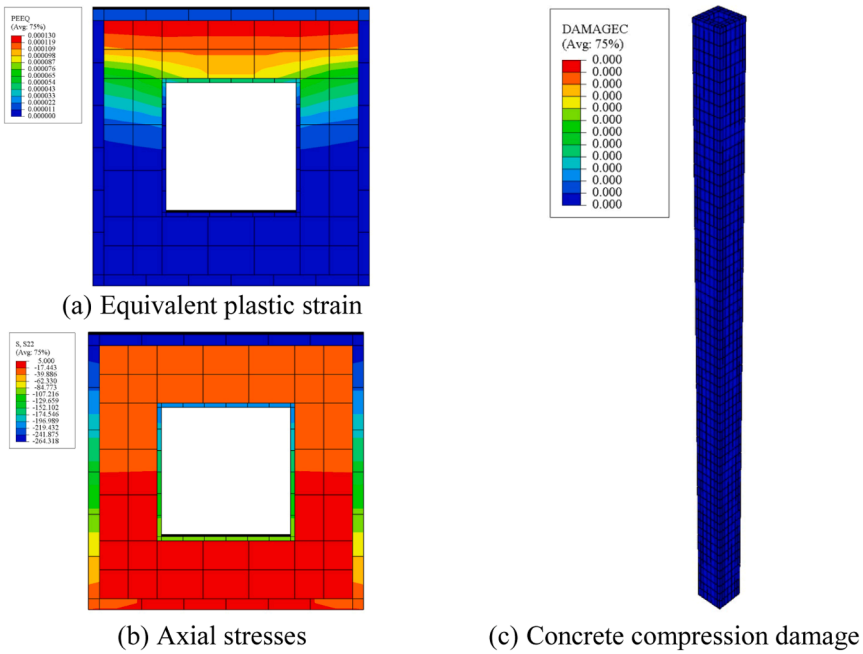

Fig. 33. Equivalent plastic strain, axial stresses, and concrete compression damage at the peak load stage for long column S12.

design models with those obtained from the numerical study. Fig. 38 presents the ultimate design strengths from each approach alongside $N_{ult,FE}$. Table 7 summarises key statistics, including the mean, coefficient of variation (COV), and the reliability index β, which is a relative measure of design integrity [61,62] and is determined as:

$$\beta = Ln\left(\frac{N{\cdot}M{\cdot}F}{\varphi}\right) \Big/ \alpha\sqrt{V_M^2 + V_N^2 + V_F^2} \tag{37}$$

Lai and Varma [63] proposed values for the terms employed in Eq. (37) for CFDST members which are employed herein. M is the mean ratio of measured-to-nominal material strength (1.10), F is the average fabrication factor (1.0), and α is the linearisation factor (0.70). N is the mean ratio of $N_{ult,FE}$ to the design prediction, while V_M, V_F and V_N represent the COVs of the material properties, fabrication process, and N, respectively. V_M and V_F are taken as 0.193 and 0.05, respectively, as recommended in [63]. A resistance factor $\varphi = 0.75$ is adopted from AISC 360–16 [38]. According to [38], a target reliability index $\beta \geq 2.5$ is required to ensure safety against global buckling failure.

As seen in Fig. 38 and Table 7, the AISC 360–16 [38] design model delivers the most accurate predictions, with the majority of results falling within ±10 % of $N_{ult,FE}$. The corresponding reliability index of $\beta = 2.63$ is also above the target value of 2.5. These findings align with the results elsewhere [31,32]. In contrast, both EC4 [39] and AS/NZS 2327 [40] tend to be conservative, underestimating the ultimate capacity of

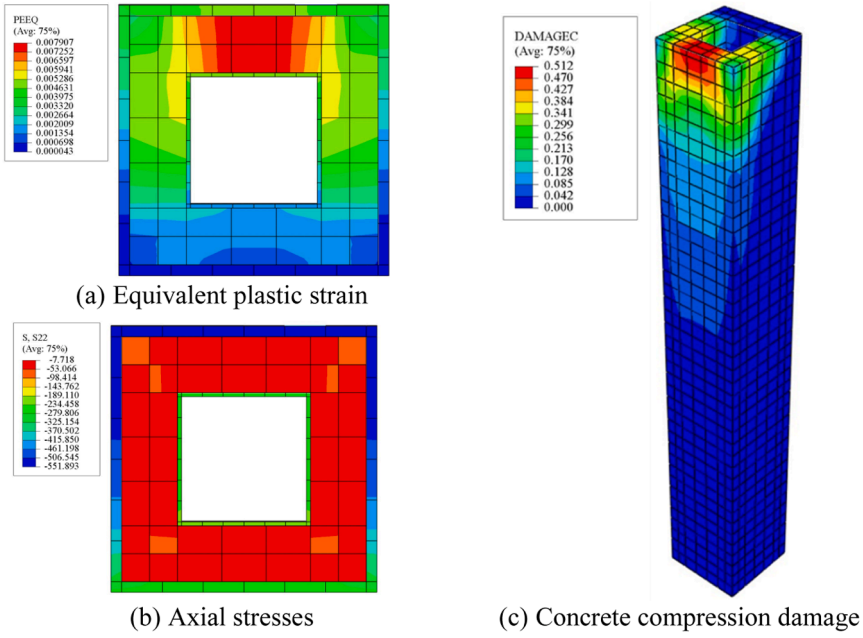

Fig. 34. Equivalent plastic strain, axial stresses, and concrete compression damage at the post-peak stage for intermediate-length column S3.

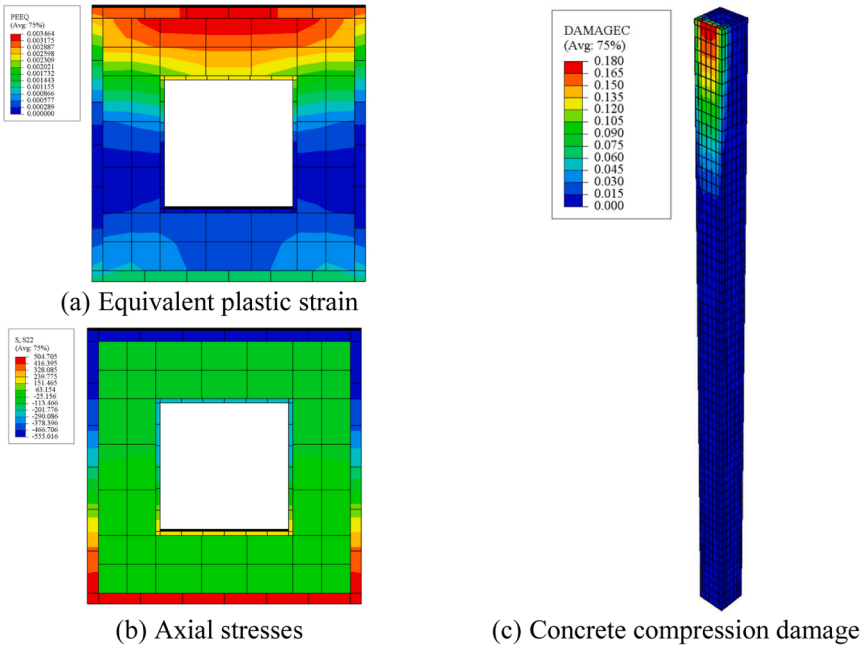

Fig. 35. Equivalent plastic strain, axial stresses, and concrete compression damage at the post-peak stage for long column S12.

the columns. The mean ratios of design strength to FE strength are approximately 0.89 and 0.78 for EC4 and AS/NZS 2327, respectively. The more accurate performance of the AISC 360–16 [38] model may be attributed to its higher estimation of the effective flexural rigidity (EI_{eff}) of the sandwiched concrete. This enhanced stiffness contributes to improved buckling resistance and more realistic strength predictions compared to the other codes.

5.5. Proposed new design models

To ensure a comprehensive and practical design framework, two different design approaches have been developed: Model 1, which provides a unified formulation across all slenderness ranges, and Model 2, which adopts a three-stage design strategy based on slenderness limits to explicitly account for distinct plastic, inelastic, and elastic failure mechanisms. As such, the first design method is a development of the original model proposed by MacPhedran and Grondin [64] for calculating the moment capacity (M_n) of laterally unbraced rolled and welded I-beams. The original expression is given as:

$$\mathrm{M_n} = \mathrm{M_p}\left(1+\bar{\lambda}^{-2n}\right)^{-1/\mathrm{n}} \tag{38}$$

where M_p is the plastic moment resistance and n is a modification factor introduced through sensitivity analysis, with an optimal value of 1.7. The non-dimensional slenderness $\bar{\lambda}$ is calculated using Eq. (15). To adapt this formulation for column design, the moment term is replaced with

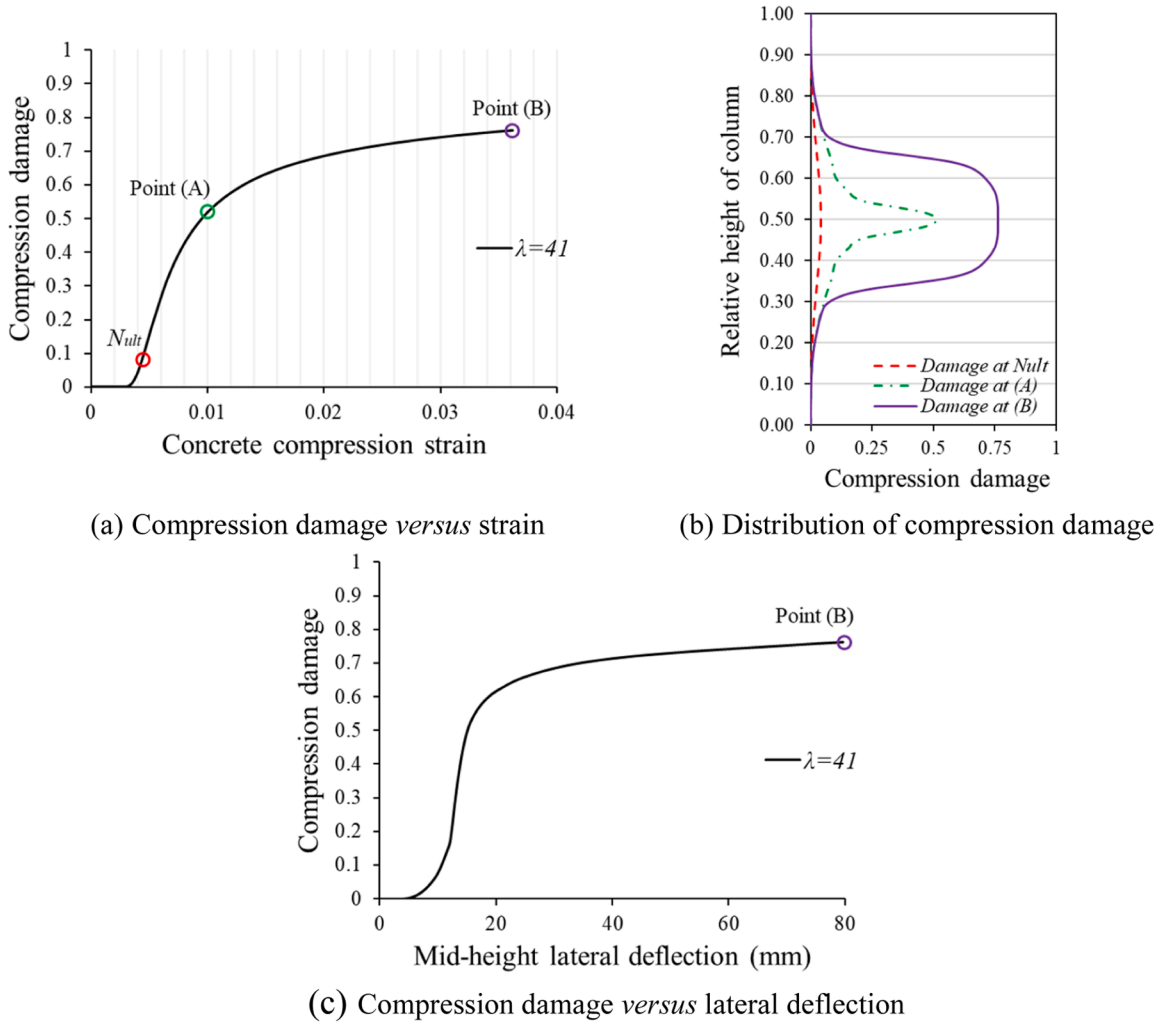

(a) Compression damage *versus* strain

(b) Distribution of compression damage

(c) Compression damage *versus* lateral deflection

Fig. 36. Development of concrete compression damage for intermediate-length column S3.

axial force and resulting in the following expression for $N_{ult,prop1}$:

$$N_{ult,prop1} = N_{pl}\left(1+\bar{\lambda}^{2n}\right)^{-1/n} \tag{39}$$

The plastic axial load capacity N_{pl} is determined using a model proposed previously [5] for axially loaded square CFDST short columns with outer stainless steel tubes. This is given by:

$$N_{pl} = \begin{cases} A_{so,eff}f_{yo} + A_{sc}f_c' + A_{si}f_{yi} & B_o/t_o \le 40 \\ A_{so,eff}f_{yo} + 0.8A_{sc}f_c' + A_{si}f_{yi} & B_o/t_o > 40 \end{cases} \tag{40}$$

where $A_{so,eff}$, A_{sc}, and A_{si} represent the effective cross-sectional areas of the outer stainless steel tube, the sandwiched concrete, and the inner steel tube, respectively. The adjustment based on B_o/t_o addresses the influence of local buckling behaviour in wider or more slender outer tubes. Table 7 presents the predicted strengths from this proposed model and it is shown that the mean value for $N_{ult,prop1}/N_{ult,FE}$ is 0.99, and the corresponding reliability index β is 2.67. These results indicate that the first proposed model offers accurate and reliable predictions for the ultimate axial strength of slender square CFDST columns with outer stainless steel tubes.

For the second developed design model, a three stage approach is proposed to calculate the ultimate design strength of square CFDST columns that fail plastically, inelastically, or elastically. The slenderness thresholds between each stage are defined as λ_p and λ_r. Specifically, λ_p is the slenderness limit below which columns fail plastically, while λ_r denotes the limit beyond which elastic buckling governs failure. For intermediate slenderness values, inelastic buckling is assumed to control the behaviour. The proposed design strength $N_{ult,prop2}$ is defined as:

$$N_{ult,prop2} = \begin{cases} N_{pl} & \lambda \le \lambda_p \\ \left(\dfrac{\lambda_r-\lambda}{\lambda_r-\lambda_p}\right)\left(N_{pl}-N_r\right)+N_r & \lambda_p < \lambda < \lambda_r \\ 0.877N_{cr,AISC2} & \lambda \ge \lambda_r \end{cases} \tag{41}$$

where N_{pl} is calculated based on Eq. (40). The slenderness limits are taken as $\lambda_r = 150/\sqrt{\frac{f_{yo}}{235}}$ and $\lambda_p = 55/\sqrt{\frac{f_{yo}}{235}}$. The reference strength N_r represents the buckling resistance at λ_r and estimated as $N_r = N_{pl}/\bar{\lambda}_r^2$.

The elastic critical buckling load is calculated according to AISC provisions as:

$$N_{cr,AISC2} = \frac{\pi^2(EI)_{eff,AISC2}}{L_e^2} \tag{42}$$

where the effective flexural rigidity is given by:

$$(EI)_{eff,AISC2} = E_{so}I_{so} + E_{si}I_{si} + C_1E_{sc}I_{sc} \tag{43}$$

C_1 is a coefficient for the concrete's effective stiffness in encased composite compression members, given as:

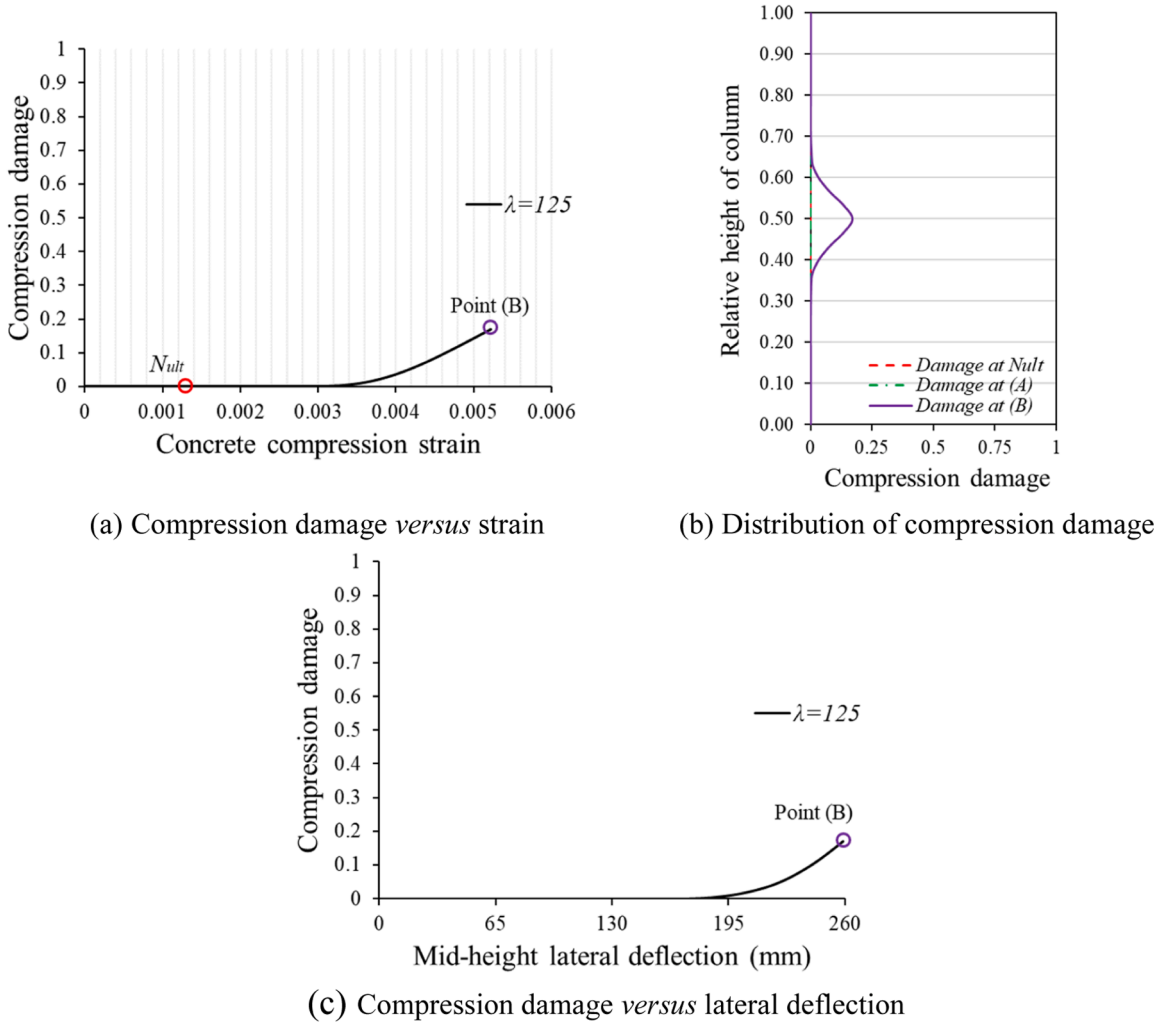

Fig. 37. Development of concrete compression damage for long column S12.

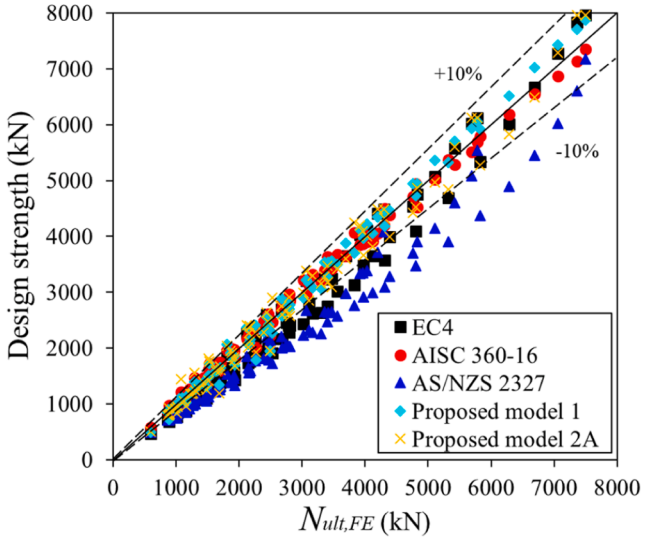

Fig. 38. Design strength values compared with $N_{ult,FE}$.

Table 7
Comparison of the different design approaches.

	EC4 [39]	AISC 360–16 [38]	AS/NZS 2327 [40]	Proposed model 1	Proposed model 2	Proposed model 2 A
	$N_{ult,EC4}/N_{ult,FE}$	$N_{ult,AISC}/N_{ult,FE}$	$N_{ult,AS}/N_{ult,FE}$	$N_{ult,prop1}/N_{ult,FE}$	$N_{ult,prop2}/N_{ult,FE}$	$N_{ult,prop2A}/N_{ult,FE}$
	Intermediate-length columns					
Mean	0.92	1.01	0.78	1.01	1.10	0.99
COV	0.085	0.046	0.064	0.066	0.081	0.092
β	3.07	2.61	4.25	2.51	2.00	2.57
	Long columns					
Mean	0.81	1.02	0.76	0.96	0.97	0.97
COV	0.037	0.05	0.044	0.049	0.12	0.097
β	4.14	2.57	4.51	2.97	2.68	2.77
	All columns					
Mean	0.89	1.01	0.78	0.99	1.04	0.98
COV	0.105	0.05	0.076	0.072	0.116	0.098
β	3.20	2.63	4.11	2.67	2.26	2.61

$$C_1 = 0.25 + 3\left(\frac{A_{so}+A_{si}}{A_{so}+A_{si}+A_{sc}}\right) \le 0.7 \quad (44)$$

Linear interpolation is used in the inelastic range between the plastic and elastic stages. The predictions using Model 2 are summarised in Table 7. While the model performs acceptably for long columns, with an average $N_{ult,prop2A}/N_{ult,FE}$ of 0.97 and a reliability index β of 2.68, it is less accurate for intermediate-length columns. For these, the average strength ratio is 1.10 and β reduces to 2.00, indicating an overestimation of capacity and insufficient reliability. To address this, a modification is proposed incorporating an index factor γ in the inelastic range to improve accuracy, giving a modified capacity equation of:

$$N_{ult,prop2A} = \begin{cases} N_{pl} & \lambda \le \lambda_p \\ \left(\frac{\lambda_r-\lambda}{\lambda_r-\lambda_p}\right)^{\gamma}(N_{pl}-N_r)+N_r & \lambda_p < \lambda < \lambda_r \\ 0.877N_{cr,AISC2} & \lambda \ge \lambda_r \end{cases} \quad (45)$$

A sensitivity analysis was conducted to determine the optimal value of γ, with results indicating that $\gamma = 2$ yields the best agreement with FE results. Table 7 presents the predictions from this improved model and it is observed that for intermediate-length columns, the average $N_{ult,prop2A}/N_{ult,FE}$ ratio is 0.99, with a reliability index of $\beta = 2.57$. When considering all column cases, the mean strength ratio is 0.98 and $\beta = 2.61$. These results confirm that Model 2 A provides accurate and reliable predictions for the ultimate axial capacity of slender square CFDST columns with outer stainless steel tubes. Fig. 39 illustrates the proposed three-stage design model (2 A) and compares the predicted capacities with finite element results for Groups G1 and G3 considered in the parametric study. Based on these comparisons, it is concluded that the proposed Model 2A is robust and well-suited for practical design applications. It is also noteworthy that a similar three-stage design methodology was adopted previously for concrete-filled stiffened steel tubular square slender columns [65].

The proposed design models are supported by detailed comparisons with finite element results (see Table 7 and Fig. 39), with reliability indices confirming their robustness. The close agreement between predicted and numerical strengths (mean ratios of 0.98–0.99 and reliability indices $\beta > 2.5$) demonstrates both the practical applicability and the rigour of the models' analytical development.

5.6. Buckling design curves

The relationship between the buckling reduction factor χ and the non-dimensional slenderness parameter $\bar{\lambda}$ for all of the examined design codes and proposed design model 1 is presented in Fig. 40. The buckling curve from AISC 360–16 [38] is included in this comparison, reformulated from Eq. (23) to express the reduction factor as:

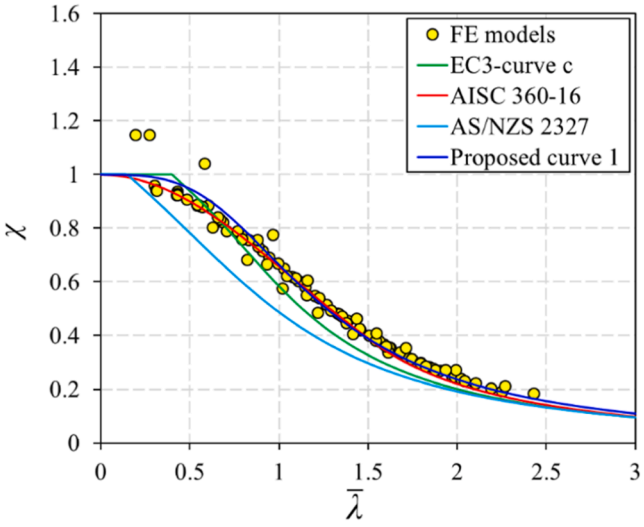

Fig. 40. Buckling reduction factor *versus* non-dimensional slenderness parameter for different design methods.

$$\chi_{AISC} = \begin{cases} 0.658^{\bar{\lambda}_{AISC}^{\,2}} & \bar{\lambda}_{AISC} \le 1.5 \\ \frac{0.877}{\bar{\lambda}_{AISC}^{\,2}} & \bar{\lambda}_{AISC} > 1.5 \end{cases} \quad (46)$$

where $\bar{\lambda}_{AISC} = \sqrt{\frac{N_{pl,AISC}}{N_{cr,AISC}}}$.

It is observed that both the proposed buckling curve—based on the formulation by MacPhedran and Grondin [64]—and the AISC 360–16 [38] design curve exhibit close agreement with the FE results. This indicates that the proposed buckling curve can be reliably adopted for calculating the strength reduction factor χ in slender square CFDST columns with outer stainless steel tubes.

6. Conclusions

This study investigated for the first time the ultimate strength and global buckling behaviour of slender square CFDST columns with an

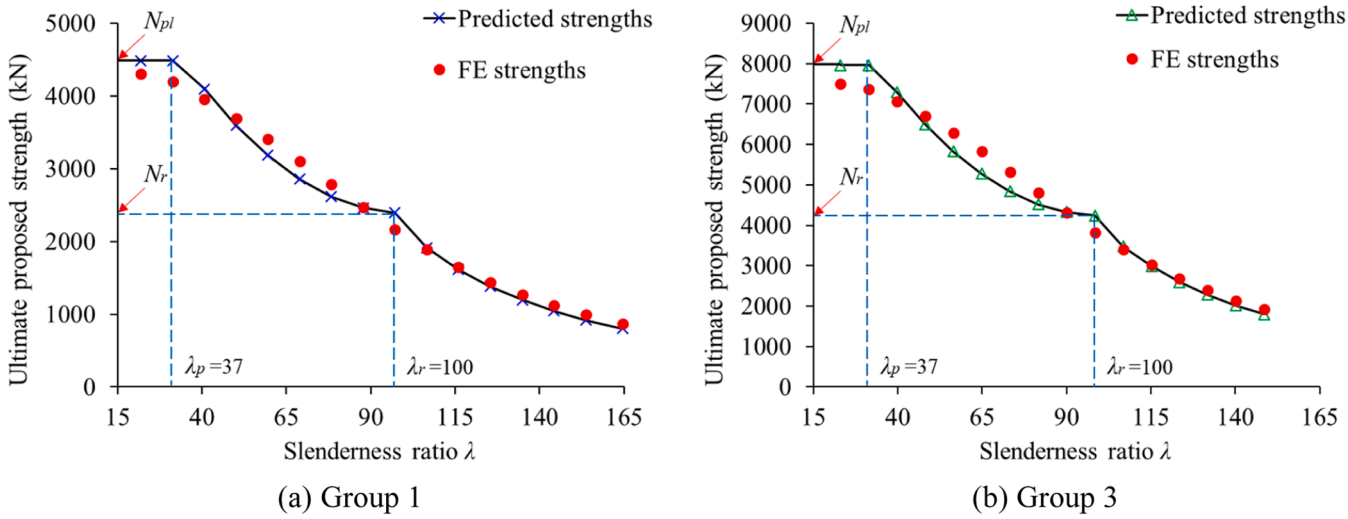

Fig. 39. Predicted ultimate strengths *versus* slenderness for groups G1 and G3.

outer stainless steel tube and an inner square carbon steel tube. The key conclusions drawn from this work are summarised as follows:

- The slenderness λ is the most influential parameter governing the structural response of slender square CFDST columns.
- Two slenderness thresholds were identified: the limit distinguishing long and intermediate-length columns is proposed as λ_r=150/$\sqrt{\frac{f_{yo}}{235}}$ while the limit separating intermediate-length and short columns is given by λ_p = 55/$\sqrt{\frac{f_{yo}}{235}}$.
- The B_o/t_o slenderness ratio of the outer tube has minimal influence on the normalised strength and lateral deflection behaviour of both intermediate-length and long CFDST columns. As failure is primarily governed by global slenderness (λ), higher B_o/t_o ratios can reduce steel usage without compromising performance.
- Concrete strength strongly affects the post-peak normalised strength–lateral deflection response of intermediate-length slender CFDST columns, but has limited impact on long columns.
- The hollow ratio has little effect on ultimate and normalised axial strengths, particularly in intermediate-length columns. However, increasing the hollow ratio significantly enhances the strength-to-weight ratio, making it a favourable design parameter.
- As global slenderness ratio (λ) increases, contact pressure at both compression and tension corners decreases. Peak contact pressure occurs at the section corners and drops to zero at the midpoints of the square cross-section sides.
- Concrete damage initiates near the peak load in intermediate-length columns during the ascending loading phase, while in long columns, damage occurs only after the peak load is reached.
- Of the current design provisions, AISC 360–16 [38] provides the most accurate predictions for slender square CFDST columns with stainless steel outer tubes, with most values within ±10 % of FE results.
- Two alternative design models are proposed and validated. Model 1 adapts a moment-based capacity formulation—originally for unbraced I-beams—to axial strength in double-skin composite columns, offering a unified method across slenderness ranges. Model 2 introduces a novel three-stage framework distinguishing plastic, inelastic, and elastic failures. A modified version, Model 2A, incorporates a sensitivity-derived parameter γ, which enhances accuracy for intermediate-length columns. Both models show strong predictive performance and practical design applicability.

Author statement

The authors' individual contributions have been outlined in Editorial Manager.

CRediT authorship contribution statement

Hassanein MF: Writing – original draft, Supervision, Resources, Project administration, Methodology, Investigation, Formal analysis, Data curation, Conceptualization. **Mohamed Amr EK:** Writing – original draft, Visualization, Validation, Methodology, Formal analysis, Data curation. **Cashell Katherine Ann:** Writing – review & editing, Visualization, Validation, Methodology. **Bock M:** Writing – review & editing, Visualization, Validation, Methodology. **YILINKE TAN:** Visualization, Resources, Investigation. **Hussein Mohamed MA:** Methodology, Formal analysis, Conceptualization. **Shao YB:** Visualization, Validation, Supervision.

Declaration of Competing Interest

The authors declare that they have no known competing financial interests or personal relationships that could have appeared to influence the work reported in this paper.

Acknowledgements

The first author acknowledges the support from the Xihua UniversityTalent Introduction Fund No. Z241152.

Appendix A

Table A
Dimensions and material properties of FE models of slender square CFDST columns

Group	*FE Model*	B_o (mm)	t_o (mm)	B_i (mm)	t_i (mm)	B_o/t_o	B_i/t_i	$\bar{\chi}$	f_{yo} (MPa)	f_{yi} (MPa)	f_c' (MPa)	L (mm)	λ	$\bar{\lambda}$	$N_{ult,FE}$ (kN)	STW $\times 10^3$
G1	S1	200	8	100	3	25	33.33	0.54	530	235	40	1400	22	0.30	4302	2.736
	S2	200	8	100	3	25	33.33	0.54	530	235	40	2000	31	0.43	4203	1.871
	S3	200	8	100	3	25	33.33	0.54	530	235	40	2600	41	0.56	3959	1.356
	S4	200	8	100	3	25	33.33	0.54	530	235	40	3200	50	0.69	3690	1.027
	S5	200	8	100	3	25	33.33	0.54	530	235	40	3800	60	0.81	3409	0.799
	S6	200	8	100	3	25	33.33	0.54	530	235	40	4400	69	0.94	3105	0.628
	S7	200	8	100	3	25	33.33	0.54	530	235	40	5000	78	1.07	2782	0.495
	S8	200	8	100	3	25	33.33	0.54	530	235	40	5600	88	1.20	2466	0.392
	S9	200	8	100	3	25	33.33	0.54	530	235	40	6200	97	1.33	2164	0.311
	S10	200	8	100	3	25	33.33	0.54	530	235	40	6800	107	1.46	1887	0.247
	S11	200	8	100	3	25	33.33	0.54	530	235	40	7400	116	1.59	1647	0.198
	S12	200	8	100	3	25	33.33	0.54	530	235	40	8000	125	1.71	1441	0.160
	S13	200	8	100	3	25	33.33	0.54	530	235	40	8600	135	1.84	1267	0.131
	S14	200	8	100	3	25	33.33	0.54	530	235	40	9200	144	1.97	1118	0.108
	S15	200	8	100	3	25	33.33	0.54	530	235	40	9800	154	2.10	992	0.090
	S16	200	8	100	3	25	33.33	0.54	530	235	40	10500	165	2.25	868	0.074
G2	S17	250	8	125	4	31.25	31.25	0.53	530	235	40	1800	23	0.31	5783	1.930
	S18	250	8	125	4	31.25	31.25	0.53	530	235	40	2500	31	0.43	5690	1.367
	S19	250	8	125	4	31.25	31.25	0.53	530	235	40	3200	40	0.55	5422	1.018
	S20	250	8	125	4	31.25	31.25	0.53	530	235	40	3900	49	0.67	5104	0.786
	S21	250	8	125	4	31.25	31.25	0.53	530	235	40	4600	58	0.79	4763	0.622
	S22	250	8	125	4	31.25	31.25	0.53	530	235	40	5300	67	0.91	4384	0.497

(*continued on next page*)

Table A (*continued*)

	S23	250	8	125	4	31.25	31.25	0.53	530	235	40	6000	75	1.03	3976	0.398
	S24	250	8	125	4	31.25	31.25	0.53	530	235	40	6700	84	1.14	3563	0.319
	S25	250	8	125	4	31.25	31.25	0.53	530	235	40	7400	93	1.26	3168	0.257
	S26	250	8	125	4	31.25	31.25	0.53	530	235	40	8100	102	1.38	2792	0.207
	S27	250	8	125	4	31.25	31.25	0.53	530	235	40	8800	110	1.50	2462	0.168
	S28	250	8	125	4	31.25	31.25	0.53	530	235	40	9500	119	1.62	2171	0.137
	S29	250	8	125	4	31.25	31.25	0.53	530	235	40	10200	128	1.74	1922	0.113
	S30	250	8	125	4	31.25	31.25	0.53	530	235	40	10900	137	1.86	1706	0.094
	S31	250	8	125	4	31.25	31.25	0.53	530	235	40	11600	146	1.98	1520	0.079
	S32	250	8	125	4	31.25	31.25	0.53	530	235	40	12300	154	2.10	1360	0.066
G3	S33	300	8	150	5	37.5	30	0.53	530	235	40	2200	23	0.31	7495	1.475
	S34	300	8	150	5	37.5	30	0.53	530	235	40	3000	31	0.43	7362	1.062
	S35	300	8	150	5	37.5	30	0.53	530	235	40	3800	40	0.54	7061	0.804
	S36	300	8	150	5	37.5	30	0.53	530	235	40	4600	48	0.65	6694	0.630
	S37	300	8	150	5	37.5	30	0.53	530	235	40	5400	57	0.77	6285	0.504
	S38	300	8	150	5	37.5	30	0.53	530	235	40	6200	65	0.88	5824	0.407
	S39	300	8	150	5	37.5	30	0.53	530	235	40	7000	73	1.00	5322	0.329
	S40	300	8	150	5	37.5	30	0.53	530	235	40	7800	82	1.11	4806	0.267
	S41	300	8	150	5	37.5	30	0.53	530	235	40	8600	90	1.22	4312	0.217
	S42	300	8	150	5	37.5	30	0.53	530	235	40	9400	98	1.34	3828	0.176
	S43	300	8	150	5	37.5	30	0.53	530	235	40	10200	107	1.45	3398	0.144
	S44	300	8	150	5	37.5	30	0.53	530	235	40	11000	115	1.56	3015	0.119
	S45	300	8	150	5	37.5	30	0.53	530	235	40	11800	123	1.68	2683	0.098
	S46	300	8	150	5	37.5	30	0.53	530	235	40	12600	132	1.79	2392	0.082
	S47	300	8	150	5	37.5	30	0.53	530	235	40	13400	140	1.91	2139	0.069
	S48	300	8	150	5	37.5	30	0.53	530	235	40	14200	149	2.02	1919	0.059
G4	S49	200	8	100	3	25	33.33	0.54	530	235	80	2600	41	0.60	4824	1.652
	S50	200	8	100	3	25	33.33	0.54	530	235	80	3800	60	0.88	4125	0.966
	S51	200	8	100	3	25	33.33	0.54	530	235	80	5000	78	1.16	3295	0.587
	S52	200	8	100	3	25	33.33	0.54	530	235	80	6200	97	1.43	2528	0.363
	S53	200	8	100	3	25	33.33	0.54	530	235	80	7400	116	1.71	1928	0.232
	S54	200	8	100	3	25	33.33	0.54	530	235	80	8600	135	1.99	1480	0.153
	S55	200	8	100	3	25	33.33	0.54	530	235	80	9800	154	2.27	1156	0.105
	S56	200	8	100	3	25	33.33	0.54	530	235	80	10500	165	2.43	1010	0.086
G5	S57	200	8	60	2	25	30	0.33	530	235	40	2600	43	0.57	4031	1.271
	S58	200	8	60	2	25	30	0.33	530	235	40	3800	63	0.83	3467	0.748
	S59	200	8	60	2	25	30	0.33	530	235	40	5000	83	1.09	2809	0.461
	S60	200	8	60	2	25	30	0.33	530	235	40	6200	103	1.35	2160	0.286
	S61	200	8	60	2	25	30	0.33	530	235	40	7400	123	1.62	1630	0.181
	S62	200	8	60	2	25	30	0.33	530	235	40	8600	143	1.88	1248	0.119
G6	S63	200	8	130	4	25	32.5	0.71	530	235	40	2600	38	0.54	3913	1.466
	S64	200	8	130	4	25	32.5	0.71	530	235	40	3800	56	0.79	3355	0.860
	S65	200	8	130	4	25	32.5	0.71	530	235	40	5000	74	1.04	2750	0.536
	S66	200	8	130	4	25	32.5	0.71	530	235	40	6200	92	1.29	2181	0.343
	S67	200	8	130	4	25	32.5	0.71	530	235	40	7400	109	1.54	1690	0.222
	S68	200	8	130	4	25	32.5	0.71	530	235	40	8600	127	1.79	1306	0.148
	S69	200	8	130	4	25	32.5	0.71	530	235	40	9800	145	2.04	1026	0.102
	S70	200	8	130	4	25	32.5	0.71	530	235	40	10500	155	2.19	898	0.083
G7	S71	200	8	100	3	25	33.33	0.54	230	235	40	2600	41	0.43	2438	0.835
	S72	200	8	100	3	25	33.33	0.54	230	235	40	3800	60	0.62	2125	0.498
	S73	200	8	100	3	25	33.33	0.54	230	235	40	5000	78	0.82	1806	0.322
	S74	200	8	100	3	25	33.33	0.54	230	235	40	6200	97	1.02	1524	0.219
	S75	200	8	100	3	25	33.33	0.54	230	235	40	7400	116	1.22	1287	0.155
	S76	200	8	100	3	25	33.33	0.54	230	235	40	8600	135	1.41	1073	0.111
	S77	200	8	100	3	25	33.33	0.54	230	235	40	9800	154	1.61	893	0.081
G8	S78	200	8	100	3	25	33.33	0.54	350	235	40	2600	41	0.48	3068	1.050
	S79	200	8	100	3	25	33.33	0.54	350	235	40	3800	60	0.71	2672	0.626
	S80	200	8	100	3	25	33.33	0.54	350	235	40	5000	78	0.93	2257	0.402
	S81	200	8	100	3	25	33.33	0.54	350	235	40	6200	97	1.15	1863	0.268
	S82	200	8	100	3	25	33.33	0.54	350	235	40	7400	116	1.38	1513	0.182
	S83	200	8	100	3	25	33.33	0.54	350	235	40	8600	135	1.60	1213	0.126
	S84	200	8	100	3	25	33.33	0.54	350	235	40	9800	154	1.82	969	0.088
G9	S85	200	3	100	3	66.67	33.33	0.52	530	235	40	1000	16	0.19	2496	2.709
	S86	200	3	100	3	66.67	33.33	0.52	530	235	40	1400	22	0.27	2496	1.935
	S87	200	3	100	3	66.67	33.33	0.52	530	235	40	3000	47	0.58	2263	0.819
	S88	200	3	100	3	66.67	33.33	0.52	530	235	40	5000	78	0.97	1684	0.366
	S89	200	3	100	3	66.67	33.33	0.52	530	235	40	8000	125	1.55	890	0.121
	S90	200	3	100	3	66.67	33.33	0.52	530	235	40	10000	157	1.93	592	0.064

Data availability

Data will be made available on request.

References

[1] Ayough P, Sulong NHR, Ibrahim Z. Analysis and review of concrete-filled double skin steel tubes under compression. ThinWalled Struct 2020;148:106495. https://doi.org/10.1016/j.tws.2019.106495.

[2] Han LH, Li W, Bjorhovde R. Developments and advanced applications of concrete-filled steel tubular (CFST) structures: members. J Constr Steel Res 2014;100:211–28. https://doi.org/10.1016/j.jcsr.2014.04.016.

[3] Le TT, Patel VI, Liang QQ, Huynh P. Numerical modeling of rectangular concrete-filled double-skin steel tubular columns with outer stainless-steel skin. J Constr Steel Res 2021;179:106504. https://doi.org/10.1016/j.jcsr.2020.106504.

[4] Wang F, Young B, Gardner L. Experimental study of square and rectangular CFDST sections with stainless steel outer tubes under axial compression. J Struct Eng 2019:145. https://doi.org/10.1061/(asce)st.1943-541x.0002408.

[5] Hassanein MF, Mohamed AEK, Hussein MMA, Shao YB, Cashell KA. Compressive behaviour and design of square concrete-filled stainless steel double-skin tubular short columns. Ocean Eng 2025;330:121206. https://doi.org/10.1016/j.oceaneng.2025.121206.

[6] Hassanein MF, Kharoob OF, Liang QQ. Circular concrete-filled double skin tubular short columns with external stainless steel tubes under axial compression. ThinWalled Struct 2013;73:252–63. https://doi.org/10.1016/j.tws.2013.08.017.

[7] Wang F, Young B, Gardner L. CFDST sections with square stainless steel outer tubes under axial compression: experimental investigation, numerical modelling and design. Eng Struct 2020;207:110189. https://doi.org/10.1016/j.engstruct.2020.110189.

[8] Hassanein MF, Mohamed AEK, Hussein MMA, Shao Y-B, Elchalakani M. Behaviour and design of axially-loaded square concrete-filled stainless steel double-skin tubular short columns with circular inner tubes. Structures 2025;76:108904. https://doi.org/10.1016/j.istruc.2025.108904.

[9] Le TT, Patel VI, Liang QQ, Huynh P. Axisymmetric simulation of circular concrete-filled double-skin steel tubular short columns incorporating outer stainless-steel tube. Eng Struct 2021;227:111416. https://doi.org/10.1016/j.engstruct.2020.111416.

[10] Wang F cheng, Han L hai, Li W. Analytical behavior of CFDST stub columns with external stainless steel tubes under axial compression. ThinWalled Struct 2018;127:756–68. https://doi.org/10.1016/j.tws.2018.02.021.

[11] Romero ML, Moliner V, Espinos A, Ibañez C, Hospitaler A. Fire behavior of axially loaded slender high strength concrete- filled tubular columns. J Constr Steel Res 2011;67:1953–65. https://doi.org/10.1016/j.jcsr.2011.06.012.

[12] Moliner V, Espinos A, Romero ML, Hospitaler A. Fire behavior of eccentrically loaded slender high strength concrete- filled tubular columns. J Constr Steel Res 2013;83:137–46. https://doi.org/10.1016/j.jcsr.2013.01.011.

[13] Espinos A, Romero ML, Serra E, Hospitaler A. Circular and square slender concrete-filled tubular columns under large eccentricities and fire. J Constr Steel Res 2015;110:90–100. https://doi.org/10.1016/j.jcsr.2015.03.011.

[14] Espinos A, Romero ML, Serra E, Hospitaler A. Experimental investigation on the fi re behaviour of rectangular and elliptical slender concrete- filled tubular columns. Thin Walled Struct 2015;93:137–48. https://doi.org/10.1016/j.tws.2015.03.018.

[15] Espinos A, Gardner L, Romero ML, Hospitaler A. Fire behaviour of concrete filled elliptical steel columns. Thin Walled Struct 2011;49:239–55. https://doi.org/10.1016/j.tws.2010.10.008.

[16] Romero ML, Ibañez C, Espinos A, Portolés JM, Hospitaler A. Influence of ultra-high strength concrete on circular concrete-filled dual steel columns. Structures 2016. https://doi.org/10.1016/j.istruc.2016.07.001.

[17] Romero ML, Espinos A, Portolés JM, Hospitaler A, Ibañez C. Slender double-tube ultra-high strength concrete-filled tubular columns under ambient temperature and fire. Eng Struct 2015;99:536–45. https://doi.org/10.1016/j.engstruct.2015.05.026.

[18] Bock M, Gardner L, Real E. Material and local buckling response of ferritic stainless steel sections. Thin Walled Struct 2015;89:131–41. https://doi.org/10.1016/j.tws.2014.12.012.

[19] Espinos A, Romero ML, Lam D. Fire performance of innovative steel-concrete composite columns using high strength steels. Thin Walled Struct 2016;106:113–28. https://doi.org/10.1016/j.tws.2016.04.014.

[20] Han LH, Xu CY, Tao Z. Performance of concrete filled stainless steel tubular (CFSST) columns and joints: Summary of recent research. J Constr Steel Res 2019;152:117–31. https://doi.org/10.1016/j.jcsr.2018.02.038.

[21] Gardner L. Stability and design of stainless steel structures – Review and outlook. Thin Walled Struct 2019;141:208–16. https://doi.org/10.1016/j.tws.2019.04.019.

[22] Tan Q, Gardner L, Han L, Song T. Fire performance of steel reinforced concrete- fi lled stainless steel tubular (CFSST) columns with square cross-sections. Thin Walled Struct 2019;143:106197. https://doi.org/10.1016/j.tws.2019.106197.

[23] Fan S, Ding X, Sun W, Zhang L, Liu M. Experimental investigation on fire resistance of stainless steel columns with square hollow section. Thin Walled Struct 2016;98:196–211. https://doi.org/10.1016/j.tws.2015.02.003.

[24] He A, Liang Y, Zhao O. Behaviour and residual compression resistances of circular high strength concrete-filled stainless steel tube (HCFSST) stub columns after exposure to fire. Eng Struct 2019. https://doi.org/10.1016/j.engstruct.2019.109897.

[25] Baddoo NR. Stainless steel in construction: A review of research, applications, challenges and opportunities. J Constr Steel Res 2008;64:1199–206. https://doi.org/10.1016/j.jcsr.2008.07.011.

[26] Gardner L. Aesthetics, economics and design of stainless steel structures. Adv Steel Constr 2008;4:113–22.

[27] Le TT, Patel VI, Liang QQ, Huynh P, Ha NS. Numerical analysis of square concrete-filled double-skin tubular columns with outer stainless-steel tube. Struct Concr 2022;23:2968–85. https://doi.org/10.1002/suco.202100649.

[28] Hassanein MF, Mohamed AEK, Hussein MMA, Shao Y. On the design and behavior of axially-compressed square concrete-filled double-skin tubular short columns for ocean engineering applications. Ocean Eng 2024;313:119396. https://doi.org/10.1016/j.oceaneng.2024.119396.

[29] Duan LX, Wang WDa, Xian W, Shi YL. Shear response of circular-in-square CFDST members: experimental investigation and finite element analysis. J Constr Steel Res 2022;190:107160. https://doi.org/10.1016/j.jcsr.2022.107160.

[30] Han L-H. Theory of concrete-filled steel tubular structures. Singapore: Springer; 2024.

[31] Hassanein MF, Kharoob OF, Gardner L. Behaviour and design of square concrete-filled double skin tubular columns with inner circular tubes. Eng Struct 2015;100:410–24. https://doi.org/10.1016/j.engstruct.2015.06.022.

[32] Zhang JH, Shao YB, Hassanein MF, Cashell KA, Hadzima-Nyarko M. Behaviour of ultra-high strength concrete-filled dual-stiffened steel tubular slender columns. Eng Struct 2024;300:117204. https://doi.org/10.1016/j.engstruct.2023.117204.

[33] Hassanein MF, Shao YB, Zhang JH, Cashell KA, Elsisy AR. Global buckling behaviour and design of square cold-formed concrete-filled dual steel stiffened slender columns. J Constr Steel Res 2024;218:108706. https://doi.org/10.1016/j.jcsr.2024.108706.

[34] Chen S, Ahmed M, Ci J, Chen W, Sennah K. Behavior and design of axially loaded square concrete-filled double steel tubular slender columns. Adv Struct Eng 2022;25:2953–65. https://doi.org/10.1177/13694332221113041.

[35] Ahmed M, Liang QQ, Patel VI, Hadi MNS. Local-global interaction buckling of square high strength concrete-filled double steel tubular slender beam-columns. ThinWalled Struct 2019;143:106244. https://doi.org/10.1016/j.tws.2019.106244.

[36] Wang W, Ji S, Shi Y. Experimental and numerical investigations on concrete-filled double-tubular slender columns under axial and eccentric loading. J Constr Steel Res 2023;201:107714. https://doi.org/10.1016/j.jcsr.2022.107714.

[37] American Institute of Steel Construction (AISC). Load and resistance factor design specification, for structural steel buildings 2010:1–612.

[38] American Institute of Steel Construction (AISC). Specification for structural steel buildings. 2016.

[39] CEN (European Committee for Standardization). Eurocode 4 - Design of composite steel and concrete structures - Part 1-1: General rules and rules for building. London: British Standards Institution; 2004.

[40] Australian/New Zealand Standard. AS/NZS 2327, Composite Structures–Composite Steel-Concrete Construction Buildings 2017.

[41] CEN (European Committee for Standardization). Eurocode 3 - Part 1-1: General rules and rules for buildings. vol. 3. 2010.

[42] CEN (European Committee for Standardization). Eurocode 3 - Part 1-4: General rules — Supplementary rules for stainless steels. 2006.

[43] Dassault Systèmes Simulia. Abaqus CAE User's Manual (6.14). 2014.

[44] Zhu T, Liang H, Lu Y, Li W, Zhang H. Axial behaviour of slender concrete-filled steel tube square columns strengthened with square concrete-filled steel tube jackets. Adv Struct Eng 2019;23:1074–86. https://doi.org/10.1177/1369433219888726.

[45] Han LH, Tao Z, Huang H, Zhao XL. Concrete-filled double skin (SHS outer and CHS inner) steel tubular beam-columns. ThinWalled Struct 2004;42:1329–55. https://doi.org/10.1016/j.tws.2004.03.017.

[46] Uy B, Tao Z, Han L. Behaviour of short and slender concrete-filled stainless steel tubular columns. J Constr Steel Res 2011;67:360–78. https://doi.org/10.1016/j.jcsr.2010.10.004.

[47] Han L-H. Concrete filled steel tubular structures-theory and practice. J Fuzhou Univ 2016;2001:34.

[48] Han L-H, Zhao X-L, Tao Z. Tests and mechanics model for concrete-filled SHS stub columns, columns and beam-columns. Steel Compos Struct nt J 2001;1:51–74.

[49] Ramberg W., Osgood W.R. Description of stress-strain curves by three parameters. Natl Advis Comm Aeronaut 1943:Technical Note No. 902.

[50] Gardner L, Yun X. Description of stress-strain curves for cold-formed steels. Constr Build Mater 2018;189:527–38. https://doi.org/10.1016/j.conbuildmat.2018.08.195.

[51] Arrayago I, Real E, Gardner L. Description of stress-strain curves for stainless steel alloys. Mater Des 2015;87:540–52. https://doi.org/10.1016/j.matdes.2015.08.001.

[52] Han LH, Yao GH, Tao Z. Performance of concrete-filled thin-walled steel tubes under pure torsion. ThinWalled Struct 2007;45:24–36. https://doi.org/10.1016/j.tws.2007.01.008.

[53] ACI 318-14. Building Code Requirements for Structural Concrete and Commentary. Farmington Hills, Michigan, USA: 2014.

[54] Zhong Tao, Zhi-Bin Wang QY. Finite element modelling of concrete-filled steel stub columns under axial compression. Appl Mech Mater 2013;351–352:138–42. https://doi.org/10.4028/www.scientific.net/AMM.351-352.138.

[55] Hassanein MF, Kharoob OF. Analysis of circular concrete-filled double skin tubular slender columns with external stainless steel tubes. ThinWalled Struct 2014;79:23–37. https://doi.org/10.1016/j.tws.2014.01.008.

[56] An Y, Han L, Zhao X. Behaviour and design calculations on very slender thin-walled CFST columns. Thin Walled Struct 2012;53:161–75. https://doi.org/10.1016/j.tws.2012.01.011.

[57] CEN (European Committee for Standardization). Eurocode 3 - Design of steel structures - Part 1-5: Plated structural elements, 3. British Standards Institution; 2007.

[58] CEN (European Committee for Standardization). Eurocode 2 - Part 1-1: General rules and rules for buildings. vol. BS En 1992. 2006.

[59] Shanmugam NE, Lakshmi B. State of the art report on steel-concrete composite columns. J Constr Steel Res 2001;57:1041–80. https://doi.org/10.1016/S0143-974X(01)00021-9.

[60] Ayrton WE, Perry J. On struts: London. Eng 1886;62:464–513.

[61] Thai S, Thai HT, Uy B, Ngo T. Concrete-filled steel tubular columns: test database, design and calibration. J Constr Steel Res 2019;157:161–81. https://doi.org/10.1016/j.jcsr.2019.02.024.

[62] Ayough P, Ibrahim Z, Sulong NHR, Hsiao PC, Elchalakani M. Numerical analysis of square concrete-filled double skin steel tubular columns with rubberized concrete. Structures 2021;32:1026–47. https://doi.org/10.1016/j.istruc.2021.03.054.
[63] Lai Z, Varma AH. High-strength rectangular CFT members: database, modeling, and design of short columns. J Struct Eng 2018;144:4018036.
[64] Macphedran I, Grondin GY. A simple steel beam design curve. Can J Civ Eng 1996; 38:141–53. https://doi.org/10.1139/L10-114.
[65] Hassanein MF, Huang W, Shao Y, Cashell KA, Elsisy AR. Confinement-based design and behaviour of concrete-filled stiffened steel tubular square slender columns. Ocean Eng 2024;304:117845. https://doi.org/10.1016/j.oceaneng.2024.117845.